SURFACE RESIDUAL STRESS EFFECTS ON STRESS CORROSION CRACKING/HYDROGEN EMBRITTLEMENT BEHAVIOR OF AISI 4340 STEEL

by

Richard A. Hays

Thesis submitted to the Faculty of the
Virginia Polytechnic Institute and State University
in partial fulfillment of the requirements
for the degree of

MASTER OF SCIENCE

in

Materials Engineering

APPROVED:

R.E. Swanson, Chairman

R.W. Hendricks

N.E. Dowling

M.R. Louthan, Jr.

December, 1988

Blacksburg, Virginia

SURFACE RESIDUAL STRESS EFFECTS ON STRESS CORROSION CRACKING/HYDROGEN EMBRITTLEMENT BEHAVIOR OF AISI 4340 STEEL

by

Richard A. Hays

Committee Chairman: R.E. Swanson
Materials Engineering

(ABSTRACT)

A series of experiments was performed in an attempt to measure the effects of surface residual stresses on the stress corrosion cracking/hydrogen embrittlement (SCC/HE) behavior of AISI 4340 steel. Stress corrosion tests were performed under load control on cylindrical and notched tensile specimens in acidified 3.5% NaCl solution. The electrochemical potential of the specimens was maintained at -0.7 V versus a saturated calomel reference electrode. Time to failure for specimens tested at various applied and residual stress levels was measured. Stress relieved specimens as well as specimens containing mechanically induced residual stresses were tested. Residual stresses were estimated using Neuber's rule and were measured using an x-ray diffraction technique. In all cases, the sum of

the applied and residual stresses was greater than zero.

Test results showed the initiation of SCC/HE cracks to be insensitive to the effects of surface residual stresses under the conditions evaluated. This is probably a result of the total time to failure criterion used to evaluate the SCC/HE tests. The extremely aggressive environment used in these experiments apparently led to rapid crack initiation, even in specimens containing compressive residual stresses. Another possible explanation of the insensitivity of this series of tests is crack initiation in the interior of the specimens below the depth of the mechanically induced residual stresses.

ACKNOWLEDGMENTS

The author would like to thank his wife Dottie and daughter Sara without whose love and support this work could not have been done. Secondly, I would like to thank the members of my committee, Dr. R.E. Swanson, Dr. R.W. Hendricks, Dr. N.E. Dowling and Dr. M.R. Louthan for their help and guidance throughout the course of my research and studies.

Many people at both Virginia Tech and David Taylor Research Center (DTRC) were responsible for making my stay at Virginia Tech both edifying and enjoyable. I would like to name a few of those in particular. At Virginia Tech, I would like to thank Ken Imrich, Bill Halley, Kathy Rohr, Ron Grzeskiewicz, Christophe Dehan, Jinmiun Jo, DeRome Dunn, and Mike Brady. At DTRC, I would like to thank Dr. Joseph Crisci, George Wacker, Tom Montemarano, Dr. John Gudas, Mike Vassilaros, Paul Ditta, Rob Mieklejohn, and Jack Saveleski.

Lastly, I would like to thank my family. Your support, encouragement, and love are greatly appreciated.

TABLE OF CONTENTS

Page No.

LIST OF FIGURES vii

LIST OF TABLES x

LIST OF ABBREVIATIONS xi

1.0 INTRODUCTION 1

2.0 BACKGROUND 3

2.1 Characteristics of Stress Corrosion Cracking 3

2.2 Mechanisms of Stress Corrosion Cracking/Hydrogen Embrittlement 4

2.3 Hydrogen Entry and Mobility in Steels 8

2.4 Residual Stresses and Stress Corrosion Cracking/Hydrogen Embrittlement 11

3.0 MATERIALS 12

3.1 Chemical Composition 13

3.2 Metallography 14

3.3 Specimens 14

4.0 EXPERIMENTAL PROCEDURE 15

4.1 Electrolyte 17

4.2 Electrochemical Tests 17

4.3 Tensile Tests 18

4.4 Acoustic Emission Measurements 19

4.5 Residual Stress Measurement 19
4.6 Residual Stress Inducement 23
4.7 Stress Corrosion Cracking/Hydrogen Embrittlement Tests 24
4.8 Prediction of Residual Stresses Using Neuber's Rule 27
5.0 RESULTS 27
5.1 Electrochemical Tests 27
5.2 Tensile Tests 28
5.3 Fractography 30
5.4 Acoustic Emission 31
5.5 Residual Stresses 32
5.6 Stress Corrosion Cracking/Hydrogen Embrittlement Tests 39
6.0 DISCUSSION 41
6.1 Total Time to Failure Criterion 42
6.2 Aggressiveness of Electrolyte 43
7.0 CONCLUSIONS 45
8.0 RECOMMENDATIONS FOR FUTURE WORK 46
REFERENCES 48
VITA 58

LIST OF FIGURES

Page No.

1. Schematic of reduction in metal/metal bond strength due to hydrogen 59
2. Anodic path dissolution model of SCC/HE 60
3. Process of hydrogen entry into metals 61
4. Metallurgical structure of AISI 4340 steel 62
5. Tempered martensite dominating AISI 4340 steel microstructure 63
6. Cylindrical tensile specimen 64
7. Notched tensile specimen 65
8. Specimen orientation with respect to plate rolling direction 66
9. Photograph of X-ray stress analyzer 67
10. Coordinate system relating stress analyzer and specimens 68
11. Schematic showing d-spacing variation as a function of orientation with respect to stress axis 69
12. Typical d versus $\sin^2\psi$ plot from TEC Model 1610 stress analyzer 70
13. Photograph of cylindrical tensile specimen SCC/HE test 71

14. Schematic of notched tensile specimen SCC/HE loading configuration 72
15. Overview photograph of notched tensile specimen SCC/HE test 73
16. Close up of notched tensile specimen SCC/HE test 74
17. Results of potentiostatic test on AISI 4340 steel 75
18. Results of potentiodynamic scan of AISI 4340 steel 76
19. Stress versus strain curve for cylindrical tensile specimens of AISI 4340 steel 77
20. Scanning electron micrograph showing ductile overload failure in cylindrical tensile specimens 78
21. Photograph of interlath or intergranular and fibrous fracture areas on SCC/HE specimens 79
22. Scanning electron micrograph of interlath or intergranular fracture on SCC/HE specimen 80
23. Scanning electron micrograph of fibrous fracture zone in center of specimens 81

24. Peak amplitude of acoustic emission versus time for specimen RH-4 82
25. Effect of reverse plasticity on Neuber's Rule predictions of residual stress 83
26. Results of SCC/HE tests for cylindrical and notched tensile specimens 84
27. Comparison of applied stress and corrected stress versus time to failure for notched tensile specimens 85
28. Schematic of surface crack initiation 86
29. Schematic of subsurface crack initiation 87
30. Schematic of stress fields in cylindrical and notched tensile specimens 88

LIST OF TABLES

Page No.

1. Chemical composition of AISI 4340 steel 13
2. Specimen identifications and testing conditions 16
3. Electrolyte used in SCC/HE tests 17
4. Stress versus strain properties of AISI 4340 steel 30
5. Residual stresses for notched tensile specimens after stress relief heat treatment 34
6. Applied loads and resulting residual stresses for notched tensile specimens 37
7. Predictions of residual stresses using Neuber's rule 38
8. Stress versus time to failure for SCC/HE tests of AISI 4340 steel 41

LIST OF ABBREVIATIONS

AISI	American Iron and Steel Institute
Å	Angstroms
d	crystal lattice plane spacing
dB	decibels
E	Young's modulus
g	gram
HCl	hydrochloric acid
HE	hydrogen embrittlement
hr	hour
i	electrical current
in	inch
kip	thousand pounds
ksi	thousand pounds per square inch
k_t	stress concentration factor
l	liter
lbs	pounds
ml	milliliter
mm	millimeter
mV	millivolts
Na_2S	sodium sulfide
psi	pounds per square inch
S	net section nominal stress

s	second
SCC	stress corrosion cracking
SCE	saturated calomel electrode
V	volts
^{o}C	degrees Celsius
^{o}F	degrees Fahrenheit
Θ	Bragg angle
σ	stress
σ_Y	yield strength
ϵ	strain
μm	micron
γ	surface free energy
λ	wavelength of incident radiation
Ψ	angle between normal to specimen surface and normal to diffracting planes
ϕ	angle between diffractometer tilt plane and chosen specimen axis

1.0 INTRODUCTION

Advances in structural design are limited by the availability of high performance engineering materials. In particular, design requirements for higher strength to weight ratio requirements for engineering materials have pushed the development of high strength steel alloys. These alloys are extensively used throughout the aircraft manufacturing, ship building, metals processing, and oil and gas exploration industries among others. Unfortunately, the high strength steel alloys generally exhibit an increased susceptibility to phenomena known as stress corrosion cracking (SCC) and hydrogen embrittlement (HE).

Numerous conferences and thousands of papers have addressed problems related to stress corrosion cracking since it was first identified as a mode of failure of engineering alloys. Technical societies such as the American Society for Testing and Materials (ASTM) and the National Association of Corrosion Engineers (NACE) have developed standardized testing procedures to determine SCC/HE susceptibility [1-6]. As a result of the increasing needs and standardization, a significant amount of data

regarding the SCC/HE susceptibility of many alloy systems, environments, and stressing conditions is available. Much of these data focus on crack growth. Standard test samples frequently contain fatigue precracks or existing stress corrosion precracks in order to avoid the initiation stage because a growth only condition represents a worst-case scenario from an engineering standpoint. Hydrogen embrittlement has more recently been thought of as a subset of SCC since stress is required to initiate and propagate cracks in a hydrogen environment [7,8,9].

Residual stresses have long been thought to influence the SCC/HE cracking performance of structures [7,10]. In many instances, SCC/HE failures have been associated with weldments or fit-up processes which resulted in large tensile residual stresses in the materials used in the structure [7,11]. Processes such as shot-peening, grit blasting, and heat treatments have long been used to modify residual stress patterns in an effort to enhance SCC/HE performance [10-13]. A greater understanding of the role of residual stresses in SCC/HE performance could aid in the formulation of specifications for processes through which maximum SCC/HE resistance is reached at the lowest cost for a given alloy system.

The purpose of the work described in this thesis was to determine the effects of surface residual stresses on the SCC/HE susceptibility of AISI 4340 steel. Time to failure as a function of applied and residual stress level during constant load tests was measured on samples exposed under electrochemical control in an acidified solution of 3.5% sodium chloride in de-ionized water.

2.0 BACKGROUND

The role of hydrogen embrittlement in service failures of engineering structures has been recognized since the early 1900's. Since that time, much research has been performed in an effort to more fully understand the conditions under which SCC/HE will occur, the mechanisms by which it occurs, and the implications on design and materials selection.

2.1 Characteristics of Stress Corrosion Cracking

In order to understand the SCC/HE phenomena, it is important to define its characteristics. The following is a brief summary of these characteristics [8,14,15]:

a. The material must experience a tensile stress

either applied or residual;

b. The material must have good resistance to general corrosion in the environment of interest;

c. The phenomena is both material and environment specific, therefore, the damaging species does not have to exist in large quantities;

d. The fracture surfaces of a material which fails by the phenomena appear brittle;

e. A threshold stress must be exceeded for cracking to occur.

Residual stresses have long been recognized as important in the SCC/HE process [7]. It has recently been shown that it is possible to produce SCC in both austenitic stainless steels and mild steels with compressive stresses under certain conditions [16,17]. SCC/HE has also been reported for torsional loading of AISI 4135 [18].

2.2 Mechanisms of Stress Corrosion Cracking/Hydrogen Embrittlement

Stress corrosion cracking can be defined as a lowering of the resistance of an alloy to cracking in response to a

combination of stress and environment. Hydrogen embrittlement can be defined as a reduction in the macroscopic ductility of an alloy with the introduction of hydrogen. Since reductions in ductility can contribute to the lowering of cracking resistance, HE can be thought of as a subset of SCC. Originally, SCC and HE were thought to be a result of distinctly different mechanisms. Although this may be the case for some types of SCC failure modes (see "pressure-expansion" below), hydrogen damage to cathodically polarized high strength steels in aqueous environments is now generally thought to be a single SCC/HE mechanism [19-22]. Several models have been put forward to explain the effects of hydrogen on the load carrying capacity or ductility of steels.

One of the first theories to be advanced was that of pressure-expansion [23,24,25]. Under this model, internal hydrogen is thought to coalesce at microcracks and voids creating extremely high pressures. These high pressures act to increase the crack or void size either through plastic deformation or by the initiation of cleavage fracture. Although this model can be successfully used to explain some failures, it is generally accepted that this model does not explain SCC/HE in high strength steels [26].

A second model relies on the lowering of the surface free energy (γ) of a metal by the adsorption of hydrogen to internal interfaces such as grain boundaries, inclusions, dislocations, and voids [27,28,29]. This is often referred to as the stress-sorption model. A reduction in surface free energy reduces the required stress for fracture using the Griffith criteria:

$$\sigma_F = \left(\frac{E*\gamma}{d}\right)^{1/2} \qquad (1)$$

where,

σ_F = fracture stress

E = elastic modulus

γ = surface free energy

d = atomic spacing

Figure (1) shows the model in schematic fashion. The measurement of the surface free energy of a fresh metal surface with adsorbed hydrogen has proven to be difficult and therefore this model has been difficult for researchers to verify and explore. It should be pointed out that, in the strictest sense, this model requires an infinitely sharp crack tip. It is therefore difficult to explain

failures in which alloys exhibit ductility using this model. However, the mechanism of lowered interfacial strength still may be applicable to materials exhibiting plasticity.

A third proposed model is known as anodic path dissolution (APD), active path corrosion (APC) or film rupture-metal dissolution [30,31]. Under this model, the protective film normally present on the metal surface is ruptured upon the application of stress. This rupture can occur due to a mismatch in ductility between the alloy and the film (brittle film) or by other plastic deformation processes such as the emergence of a slip step at the metal/film interface. The small, newly exposed regions are anodic to the rest of the surface, especially the crack faces [8]. Some dissolution of the anodic areas may occur during the repassivation process. A schematic of this process is shown in Figure (2).

A fourth important model is that of hydrogen enhanced plasticity [32]. High-fugacity hydrogen has been found to decrease the resistance to dislocation motion within a grain [26]. Therefore, the model proposes that the role of hydrogen is to aid in plastic deformation processes ahead

of the crack tip which lowers cracking resistance.

2.3 Hydrogen Entry and Mobility in Steels

In order for SCC/HE to occur, hydrogen must be present in the host lattice in sufficient quantities to lower the threshold stress for cracking. There is little or no evidence that hydrogen adsorbed onto external surfaces causes embrittlement [33]. In the case of the work described here, the hydrogen entered the host lattice from the aqueous environment via cathodic polarization of the steel specimens.

The steps involved in entry of hydrogen into the host lattice in aqueous solutions include at least [26,34]:

a) Arrival of water molecule at metal surface;
b) Reduction of water molecule ($H_2O \rightarrow H^+ + (OH^-)$);
c) Adsorption of hydrogen ion onto external surface;
d) Absorption of hydrogen into host lattice;
e) Localization of [H] to critical regions within the host lattice.

A schematic of this process is shown in Figure (3). The rate-limiting step in the embrittlement process is

dependent on several factors including overpotential, pH and composition of the solution, chemical state of the metal surface, local atomic configuration of the metal surface, metallurgical condition, and temperature [26,35].

Once the hydrogen is absorbed, it is attracted to heterogeneities within the lattice. These include local stress fields, grain boundaries, inclusions, dislocations, and voids [26,35,36]. Movement towards these heterogeneities can be rather rapid (hydrogen diffusivity in high strength steel at room temperature is on the order of 10^{-9} cm^2/sec [37]). However, not all of the hydrogen within the lattice is available to cause damage since a significant amount can be trapped in innocuous sites [33,38].

Hydrogen trapping was first suggested in 1949 [39] and since then it has been widely substantiated [35,36,40-45]. Trapping sites in iron-based alloys include dislocations [46,47], grain-boundaries [35,43], voids [45], particle/matrix interfaces [36,43], and stress fields [36]. Essentially, these traps act as sinks for free lattice hydrogen and have the effect of reducing hydrogen permeability and thus SCC/HE susceptibility. Different

trapping sites will have varying strengths or ability to attract and hold hydrogen. Additionally, some trapping sites may be irreversible in nature. Hydrogen which has migrated to these sites cannot become free lattice hydrogen. If this irreversible trap is innocuous, the hydrogen contained within it is not available to contribute to the damage process.

The role of H_2S is to increase the rate of hydrogen absorption which effectively reduces the resistance of high strength steels to SCC/HE [26,48,49]. This has been a continuing problem in the oil and gas industry. There are two schools of thought as to the role of H_2S in increasing SCC/HE susceptibility. The first is that the presence of H_2S poisons the hydrogen recombination reaction at the metal surface [12,48]. More H^+ ions are then available for absorption into the lattice. The second is that H_2S promotes the formation of a complex hydroxide film which replaces the film normally found on the alloy [26]. Hydrogen is thought to more easily adsorb to and permeate this film resulting in higher hydrogen concentrations in the lattice.

2.4 Residual Stresses and Stress Corrosion Cracking/Hydrogen Embrittlement

Stress corrosion cracking/hydrogen embrittlement failures in which residual stresses played a major role have been widely reported [7,10,11,12]. Residual stresses exist in all engineering structures. These stresses can be as a result of materials processing such as rolling, extruding, forging, shot-peening, and heat treatment [12]. They may also be a result of joining processes such as welding, bolting, and riveting [7,10]. Finally, they may be a result of fit-up procedures during the construction of a structure. Although these stresses are at or below the material yield stress, they are sufficient to cause cracking and failure.

Modification of residual stress patterns is an efficient and effective strategy for combating SCC/HE [10,12,50]. Processes which induce compressive residual stresses in surfaces by mechanical deformation such as shot-peening or grit blasting have been shown to be effective in reducing SCC/HE attack [13,51]. Additionally, residual stress pattern modification through heat treatment is also widely used, especially for weldments. Processes for changing the residual stress patterns in piping systems

have been proposed in order to lessen the damaging effects of tensile residual stresses and, indeed, to take advantage of the beneficial effects of compressive residual stresses [52].

Although the general relationships between residual stresses and SCC/HE are well known, ie. compressive residual stresses enhance SCC/HE performance, quantitative relationships have been not been established. This is primarily due to the difficulty in measuring the orientation and magnitude of residual stresses. In 1982, the National Materials Advisory Board of the U.S. Nuclear Regulatory Commission stated, "The potential role of residual stresses on environmentally assisted cracking behavior in as-welded steel structures is perhaps the single most complicating aspect of designing against corrosion"[10].

3.0 MATERIALS

The material used in this investigation was AISI 4340 steel which has a UNS designation of G43400. AISI 4340 steel is a low alloy, high-hardening steel used in a wide range of applications. The material was delivered in the form of a one-inch thick plate. The final heat treatment

during production consisted of annealing for one hour between 1525 ^{o}F and 1575 ^{o}F, furnace cooling at 50 ^{o}F per hour to 600 ^{o}F, and air cooling to room temperature.

3.1 Chemical Composition

The chemical composition of this steel is specified under ASTM A322 [53]. The chemical composition for the plate which was evaluated within specification for all elements, Table (1).

Table (1). Chemical composition of AISI 4340 steel.

ELEMENT	SPECIFICATION	TEST MATERIAL
Fe	Bal.	Bal.
C	0.38 - 0.43	0.41
Mn	0.60 - 0.80	0.74
P	0.035 max	0.009
S	0.040 max	0.016
Si	0.15 - 0.35	0.21
Ni	1.65 - 2.00	2.00
Cr	0.70 - 0.90	0.74
Mo	0.20 - 0.30	0.26
V		0.05

3.2 Metallography

Metallography was performed in three mutually perpendicular directions with respect to the plate rolling direction, Figure (4). "Stringers" elongated in the rolling direction are clearly visible. These stringers are nonmetallic inclusions, primarily manganese sulfides, are retained in the metal upon solidification. The tempered martensitic laths which dominate the microstructure are shown at higher magnitude in Figure (5).

3.3 Specimens

Cylindrical and notched specimens, Figures (6) and (7), for use in both tensile and stress corrosion experiments were machined from a one inch thick plate. The cylindrical specimens were machined with the long axis parallel to the plate rolling direction while the notched specimens were oriented such that the long axis of the specimen was transverse to the rolling direction of the plate, Figure (8). An additional specimen was taken from a notched tensile specimen which had been previously tested. This specimen was used in the potentiostatic and potentiodynamic evaluations.

After machining, it was necessary to remove as much of the existing residual stress as possible. Therefore, all specimens were wrapped in stainless steel foil and stress relieved at 593 ^{o}C (1100 ^{o}F) for six hours in a laboratory furnace. The specimens were then allowed to furnace cool to room temperature. The foil was used to promote even cooling of the sample by reducing convection and to reduce oxidation of the specimen surfaces. In spite of the use of the foil, a significant oxide formed on the specimen surfaces during the stress relief procedure. Removal of this oxide was performed by soaking the specimens in a 10% hydrochloric acid solution until it was loosened sufficiently for removal by a cotton-tip swab.

4.0 EXPERIMENTAL PROCEDURE

The intent of the series of experiments performed during this investigation was to evaluate the effects of surface residual stresses on the SCC/HE behavior of AISI 4340 steel. In order to do this, four types of tests were performed. First, the electrochemical properties of the material were measured in the electrolyte of interest. Second, the stress vs. strain behavior was measured for the material in the stress relieved condition. The SCC/HE

characteristics of both cylindrical and notched specimens in the stress relieved condition were then measured. In the fourth and final test, the SCC/HE characteristics of notched tensile specimens containing mechanically induced residual stresses were evaluated. Table (2) provides a complete listing of the specimen identifications and test conditions.

Table (2). Specimen identifications and testing conditions.

SPECIMEN ID	SPECIMEN GEOMETRY AND TEST CONDITION
RH-14E	Electrochemical tests
RHTEN1	Cylindrical specimen, mechanical properties
RHTEN3	Cylindrical specimen, mechanical properties
RHTEN4	Cylindrical specimen, mechanical properties
RH-1	Notched specimen, SCC/HE, compressive RS
RH-2	Notched specimen, SCC/HE, compressive RS
RH-3	Notched specimen, SCC/HE, tensile RS
RH-8	Notched specimen, SCC/HE, stress relieved
RH-10	Notched specimen, SCC/HE, stress relieved
RH-13	Notched specimen, SCC/HE, stress relieved
RH-14	Notched specimen, SCC/HE, stress relieved
RHT-1	Cylindrical spec., SCC/HE, stress relieved
RHT-2	Cylindrical spec., SCC/HE, stress relieved
RHT-3	Cylindrical spec., SCC/HE, stress relieved

4.1 Electrolyte

The electrolyte used in this investigation was 3.5% sodium chloride (NaCl) in de-ionized water acidified with HCl to a pH of approximately 1.0. Sodium sulfide (Na_2S) was added to poison the hydrogen gas recombination reaction at the specimen surface. The solution was prepared using the quantities shown in Table (3).

Table (3). Electrolyte used in SCC/HE tests.

AMOUNT	COMPONENT
3.0 l	de-ionized water
105 g	NaCl
14.0 ml	HCl
0.4 g	Na_2S

This electrolyte was chosen in order to produce rapid SCC/HE.

4.2 Electrochemical Tests

A portion of notched tensile specimen RH-14 was removed after SCC/HE testing for use in the electrochemical tests. The specimen was prepared such that an area of approximately 400 mm^2 (0.62 in^2) would be exposed to the

electrolyte. This area was ground with 600 grit abrasive paper, cleaned with 10% HCl, and degreased with hexane prior to testing.

A potentiostatic test was performed on the specimen to determine the open circuit corrosion potential of the material in the electrolyte. A computer-controlled EG&G Princeton Applied Research Potentiostat/Galvanostat model 273 was used to monitor the test. The potential with respect to a saturated calomel reference electrode (SCE) was measured at five second intervals during a 1000 second period while the specimen was exposed to the electrolyte.

Immediately following the potentiostatic test, a potentiodynamic scan was performed on the same specimen. The potential was ramped at 0.1 mV/s between limits of -0.8 V to -0.4 V versus SCE and the corresponding current was measured.

4.3 Tensile Tests

Three quasi-static tensile tests were performed on 0.25 in. cylindrical tensile specimens, Figure (6). Testing was performed in displacement control on a computer controlled Materials Testing Systems (MTS) closed loop servohydraulic

machine with a 20,000 lb load capacity. The variable range load cell was set at 10,000 lb maximum for the tests. Elongation was measured using an extensometer with a 0.25 in. maximum displacement capacity. The displacement rate was approximately 0.01 in/min.

4.4 Acoustic Emission Measurements

The notched tensile specimens were monitored for acoustic emission during the tests using a Physical Acoustics Corporation model 3104 data acquisition and analysis system. A single transducer was attached to the specimen just above the test section to collect data. A guard sensor was placed on each of the specimen grips in order to eliminate acoustic emissions emanating from the load train. A threshold level of 0.5 V and a gain of 34 dB were used as parameters in acquiring the data. Amplitude, energy, rise time, and counts for each event were acquired with a maximum speed of 10 events per second.

4.5 Residual Stress Measurement

Residual stress measurement was performed using an X-ray diffraction technique with a Technology for Energy Corporation (TEC) model 1610 Mobile X-ray Stress Analyzing

System. A photograph of the stress analyzer is shown in Figure (9) and a coordinate system relating the stress analyzer and the specimen is schematically shown in Figure (10).

The stress analysis is based on measurement of lattice strain. X-rays are used to measure the crystal lattice spacing utilizing Bragg's Law:

$$n \lambda = 2d\sin\theta \qquad (2)$$

where,

n = positive integer

λ = wave length of incident radiation

d = lattice spacing

θ = Bragg angle (half the angle between the incident and diffracted beam)

for a specific set of lattice planes. Grains in the same relative location but with different orientations with respect to the stress axis are measured. This is done by tilting the X-ray source and detector through an angle, ψ. The spacing of a given set of lattice planes will vary with the orientation of a grain with respect to the stress axis, Figure (11). Therefore, the d-spacing can be expected to be a function of the ψ-angle.

It may be shown that the relationship between stress and the lattice spacing at varying ψ-angles for isotropic, fine-grained materials having no preferred microstructural orientation follows the equation [54]:

$$\frac{d_{\phi\psi}-d_0}{d_0} = \frac{1+\nu}{E}\{\sigma_{11}\cos^2\phi+\sigma_{12}\sin 2\phi+\sigma_{22}\sin^2\phi-\sigma_{33}\}\sin^2\psi + \frac{1+\nu}{E}\sigma_{33}-\frac{\nu}{E}(\sigma_{11}+\sigma_{22}+\sigma_{33}) + \frac{1+\nu}{E}\{\sigma_{13}\cos\phi+\sigma_{23}\sin\phi\}\cdot\sin 2\psi . \quad (3)$$

where,

d_o = lattice spacing of unstrained material

$d_{\phi,\psi}$ = measured lattice spacing at diffractometer tilt angle,

ψ = angle between normal to specimen surface and normal to diffracting planes

ϕ = angle between diffractometer tilt plane and chosen specimen axis

σ_{ij} = stress in ij direction

During the experiment, the diffractometer tilt plane is set parallel to the direction in which the stress is to be measured. Under this condition, $\psi = 0^o$. The slope of a

plot of the measured d-spacing versus $\sin^2\psi$ is then directly related to the stress ($\sigma_{11} - \sigma_{33}$) plus a constant. At $\psi=0^o$ in iron, 95% of the diffracted intensity comes from the first 17 μm of material [54]. Since triaxial stresses cannot exist at a free surface, σ_{33} is taken to be small with respect to σ_{11} and neglected. The slope of the plot can therefore be thought to represent the stress σ_{11}. A split in the d vs. $\sin^2\psi$ plot is interpreted as indicative of a shear stress in the material. During the course of this research, the shear stresses were found to be small and relatively constant from specimen to specimen. Therefore, shear stresses were not included in the analysis of results.

Chromium radiation (λ = 2.29 Å) and a Bragg angle (2θ) of 156^o were chosen to measure the diffraction from the (211) planes for the AISI 4340 steel. Five ψ-angles were measured. These included -35.0^o, -18.0^o, 0.0^o, 18.0^o, and 35.0^o. The x-ray tube power supply was set at 35 kV and 1.7 mA. A rectangular beam collimator with dimensions 0.5mm X 5.0 mm was used. A count time of 1000 s was used at the ψ =0^o position. Count times at other ψ-angles were calculated to account for sample absorption and increased to yield approximately the same number of total

counts as were collected at $\Psi = 0^{o}$. Data were collected in the vicinity of the Bragg angle using a position-sensitive x-ray detector and were digitized into 256 channels. The data were then fed to a DEC LSI 11/23 Plus computer for analysis and output. A typical plot is shown in Figure (12).

X-ray residual stresses measurements were not performed on the cylindrical tensile specimens. A negligible residual stress level was assumed after a control specimen of the same material given the same heat treatment resulted in residual stress measurements of approximately zero. X-ray residual stress measurements were performed on the notched tensile specimens at the root of the notch on both sides of the specimen.

4.6 Residual Stress Inducement

After the stress relief procedure and the removal of the oxide, residual stresses were mechanically induced in some of the notched tensile specimens. Tensile residual stresses were induced in specimen RH-3 by compressing the specimen in a 50 kip capacity servohydraulic MTS machine in load control to 15600 lb. At this load, the material at the notch root underwent plastic deformation. Upon release of

the applied load, the elastic stresses in the bulk of the specimen acted to produce a tensile residual stress at the notch root. In a similar manner, compressive residual stresses were induced in specimens RH-1 and RH-2 by plastically deforming the notch root in tension. The tensile loadings of 14500 lb and 15500 lb respectively were performed in a 20 kip capacity servohydraulic MTS machine.

4.7 Stress Corrosion Cracking/Hydrogen Embrittlement Tests

Stress corrosion cracking/hydrogen embrittlement tests were performed on both cylindrical and notched tensile specimens. The tests were performed such that the test sections of both types of specimens were exposed to the electrolyte. The specimens were held at a constant potential of -0.7 V vs. SCE using an EG&G Princeton Applied Research model 173 potentiostat. Graphite counter electrodes were used.

The cylindrical tensile specimens were tested in the stress relieved condition on a 20,000 lb capacity MTS servohydraulic testing machine operated in load control. Screw-type grips were used to attach the specimens to the load train. Load levels were calculated to match the notch

stress levels used in testing the notched tensile specimens. Figure (13) is a photograph of the test configuration. Electrolyte was supplied to the chamber surrounding the specimen at a rate of approximately of 3 l/hr. The specimen gage section was fully immersed throughout the tests. Time to failure was measured as a function of applied stress. Failure was defined as separation of the specimen into two pieces.

The notched tensile specimens were tested in a Riehle Testing Machines 12,000 lb capacity dead weight loading machine which is primarily intended for creep testing. Both stress relieved specimens and specimens with mechanically induced residual stresses were tested. A schematic of the test configuration is presented in Figure (14). Photographs of a test in progress are shown in Figures (15) and (16). Pin loading was used in an effort to reduce the amount of bending applied to the specimens during testing. The specimens were held at a constant potential of -0.7 V vs. SCE throughout the tests.

Steel weights were added in 20 lb increments across a lever with a 20-to-1 load ratio in order to apply load to the specimens. Load levels were calculated in order to vary the notch stress levels from 30% to 110% of the yield

strength of the material. Notch stress was calculated using:

$$\sigma = k_t S \qquad (4)$$

where,

σ = notch stress

k_t = stress concentration factor (2.02)

S = net section nominal stress.

for cases where the notch stress was below the yield strength. For the single specimen where the applied load exceeded the yield strength, Neuber's rule [55] was used to calculate the notch stress. Neuber's rule can be stated as the following:

$$\sigma\epsilon = \frac{(k_t S)^2}{E} \qquad (5)$$

where,

σ = notch stress

ϵ = notch strain

S = net section nominal stress

k_t = stress concentration factor (2.02)

E = Young's modulus

The notch stress for this specimen was thus adjusted to

97% of the 0.2% offset yield strength or 177.5 ksi. As with the cylindrical specimens, time to failure as a function of notch stress was measured. Failure was defined as separation of the specimen into two pieces.

4.8 Prediction of Residual Stresses Using Neuber's Rule

Neuber's Rule, Eqn. (5) can also be used to predict residual stresses at stress concentrations given a nominal net section stress, stress concentration factor, and material stress versus strain behavior. Equation (5) describes a series of hyperbolas in stress/strain space for different nominal net section stresses. The intersection of the stress versus strain curve and the hyperbola for a given nominal net section stress gives the notch stress and strain values for that nominal net section stress. Residual stresses can be predicted by applying Neuber's Rule once on loading and again on unloading.

5.0 RESULTS

5.1 Electrochemical Tests

The open circuit corrosion potential of the AISI 4340 steel was determined to be -0.528 V. Figure (17) shows the

potential as a function of time for the 1000 s test. While a longer test may have resulted in a slightly lower corrosion potential, the figure indicates that any decrease in potential with increasing time would have been extremely small.

The potentiodynamic scan showed no discontinuities in the potential vs. current relationship between -0.7 V and the corrosion potential, Figure (18). This indicates that a single corrosion process is occurring between the two potentials. The open circuit corrosion potential (point at which i=0) as measured using this method is slightly higher than that measured using the potentiostatic method. This may be due to a rate effect in the ramping of the potential and is not considered to be significant.

5.2 Tensile Tests

Stress versus strain curves for the first 5% strain are shown for the three quasi-static tensile tests in Figure (19). The curves are characterized by a low strain hardening exponent similar to that reported elsewhere [56,57]. For the purposes of Neuber's rule calculations, the stress vs. strain curves were fit in two ranges. In

the elastic range ($\sigma < \sigma_Y$), the data were fit to Hooke's Law:

$$\sigma = E\epsilon \tag{6}$$

where,

σ = true stress

E = Young's modulus

ϵ = true strain

After the onset of plasticity ($\sigma > \sigma_Y$), a power law equation of the form:

$$\sigma = A\epsilon^s \tag{7}$$

where,

σ = stress

A = constant, stress at $\epsilon = 1.0$

s = strain hardening exponent

was fit to the data. Results of the three tests are tabulated below.

Table (4). Stress vs. strain properties of AISI 4340 steel.

SPEC. ID.	YIELD STRENGTH (ksi)	ULT. STRENGTH (ksi)	E (ksi)	A (ksi)	s
RHTEN1	171.3	183.3	3.0e4	224.6	0.0575
RHTEN3	166.8	182.1	2.8e4	230.0	0.0658
RHTEN4	180.5	183.6	2.8e4	231.2	0.0649
AVG.	172.9	183.0	2.9e4	228.6	0.0630

The notched and cylindrical specimens were taken from the plate in different orientations, Figure (8). Unpublished data for the steel evaluated in these tests shows less than 1 ksi difference in yield strength between the long and transverse orientations. It is therefore thought that these results for cylindrical specimens are applicable to the notched specimens.

5.3 Fractography

The fracture mode of the quasi-static tensile test specimens was ductile overload. This was confirmed by scanning electron microscopy, Figure (20). Another feature of these fracture surfaces was the shallow trough-like

regions. These regions are a result of the non-metallic inclusions disbonding from the metallic matrix [58].

The fracture surfaces of both types of SCC/HE specimens were characterized by two zones as shown in Figure (21). A zone of interlath or intergranular fracture, Figure (22), rings the specimen fracture surface. Some secondary cracking is also apparent. This attack is indicative of SCC/HE. The center of the fracture surface is a ductile fracture zone, Figure (23), similar to that observed in the quasi-static tensile tests.

5.4 Acoustic Emission Measurements

The acoustic emission results were inconclusive in terms of detection of crack initiation. An example of a test record is given in Figure (24). Peak amplitude for an 10 s window is plotted versus time during the test. Acoustic emission events occurred throughout the test with approximately a constant peak amplitude until failure was imminent. The energy of the acoustic emission followed this same trend.

Two of the specimens had a significantly lower density of acoustic emission events during the course of the tests.

The peak amplitude and energy levels were similar to those of the specimens which exhibited a high density of acoustic emission. Comparisons of the times to failure and fracture surfaces of the specimens exhibiting a high density of acoustic emission with those exhibiting a low density showed no discernible differences.

5.5 Residual Stresses: Measurements and Predictions

As mentioned above, all specimens were given a stress relief heat treatment prior to any testing. Residual stresses for the cylindrical tensile specimens were inferred from measurements of a 1 in. cube of the same material given the same heat treatment. A single face of the cube was chosen for residual stress measurement. Prior to the stress relief heat treatment, this face had a residual stress level of -73.1 +/- 1.6 ksi. The large compressive residual stress was probably a result of prior machining or sawcutting of the cube. After the stress relief heat treatment, residual stresses were measured in two orthogonal directions on the cube face. The residual stress level in one orientation was -5.1 +/- 1.7 ksi and in the other was -3.6 +/- 2.2 ksi. It can safely be assumed, therefore, that the cylindrical tensile specimens contained

negligible residual stresses after the stress relief heat treatment.

The residual stress levels at the notch roots of all the notched tensile specimens were measured after the stress relief heat treatment. Sides of the specimens were arbitrarily labeled "1" and "2" after removal from the furnace. Two measurements were then made on each notch of each specimen and averaged. The results are given in Table (5).

Table (5). Residual stresses for notched tensile specimens after stress relief heat treatment.

SPEC. ID.	SIDE	AVG. RES. STRESS* (ksi)
RH-1	1	-8.5
RH-1	2	-11.8
RH-2	1	-4.7
RH-2	2	-11.2
RH-3	1	-2.8
RH-3	2	-6.1
RH-4	1	-2.2
RH-4	2	-8.2
RH-8	1	-6.6
RH-8	2	+0.9
RH-10	1	-3.4
RH-10	2	-18.9
RH-12	1	-80.4
RH-12	2	-79.2
RH-13	1	+7.1
RH-13	2	-15.0
RH-14	1	-16.1
RH-14	2	-1.2

* + = tensile, - = compressive

Residual stresses ranged from approximately -20 ksi to +8 ksi. Additionally, a fairly large side-to-side variation was noted for some of the specimens. This side-to-side

variation was not a result of counting statistics errors since these errors had magnitudes on the order of 2 ksi. While it is not known why this variation occurred, it may be due to differential cooling rates resulting from the location of the particular specimen in the furnace. As will be seen later, these variations in residual stress are small in comparison with the mechanically induced residual stresses.

In some cases, residual stresses were measured prior to and after the removal of the oxide which formed during the stress relief heat treatment. The differences in measured residual stresses before and after removal of the oxide were negligible and probably attributable to variations in alignment of the specimens during measurement. This result is potentially important in two respects. First, accurate and consistent residual stress measurements can be made through a thin oxide layer. Second, exposure to a fairly strong acid for a short period of time does not affect the macroscopic residual stress. It must be noted that these specimens were intentionally treated to remove stress gradients and exposure to acid might alter the stress state in specimens containing gradients.

For the specimens in which residual stresses were

induced, the specimens were measured prior to and after the mechanical deformation. The specimens were initially loaded to net section nominal stresses of +103.6 ksi, +111.7 ksi, and -103.6 ksi for specimens RH-1, RH-2, and RH-3 respectively. These levels were calculated using Neuber's rule, Eqn. (5), to produce residual stress levels of -36.4 ksi, -51.2 ksi, and +36.4 ksi respectively. However, measurement of the specimens revealed no change in the residual stress levels.

There are two possible explanations for this result. The first is an elevation of the yield strength due to the biaxial stress state in the notch. Yield strengths can be elevated up to 15% under biaxial stress [59]. If the yield strength was elevated, the notch may not have undergone any plastic deformation on loading and therefore did not contain residual stresses on unloading. The second explanation is that the small initial compressive residual stresses in the specimens prior to loading were not taken into account in the calculations. These compressive stresses may have been sufficient to keep the notch root elastic under the applied stresses thereby resulting in no residual stresses.

A second series of loadings was performed to increased stress levels. At these levels, significant residual stresses were induced and subsequently measured. Table (6) presents the applied loads nominal net section stress levels, and measured residual stresses for these specimens.

Table (6). Applied Loads and Resulting Residual Stresses for Notched Tensile Specimens

SPECIMEN ID	APPLIED LOAD* (kip)	NET SECT NOMINAL STRESS (ksi)	RESIDUAL STRESS* (ksi)	
			SIDE 1	SIDE 2
RH-1	+14.5	+130	-64.7	-76.4
RH-2	+15.5	+140	-77.7	-74.7
RH-3	-15.6	-141	+39.0	+78.3

* + = tensile, - = compressive

Neuber's Rule was again used in an effort to predict the residual stress levels attained in the specimens. In all cases, Neuber's Rule predicted residual stresses larger in tensile or compressive magnitude than those measured. Several combinations of the measured stress/strain parameters (A and s) were used to try to determine the impact of material variability on the residual stress predictions. Table (7) summarizes the results of the Neuber's rule calculations.

Table (7). Predictions of Residual Stress using Neuber's Rule.

STRESS/STRAIN PARAMETERS	PREDICTED RESIDUAL STRESS* (ksi)		
	RH-1	RH-2	RH-3
Averages A=228.6 ksi, s=0.0630	-87.5	-104.1	+105.1
High Measured A=230.0 ksi, s=0.0658	-88.43	-105.0	+105.5
Low Measured A=224.6 ksi, s=0.0575	-86.7	-103.2	+104.3
High A, Low s A=231.2 ksi, s=0.0575	-81.6	-98.3	+100.0
Low A, High s A=224.6 ksi, s=0.0658	-92.2	-108.7	+110.7

* + = tensile, - = compressive

These results indicate that the difference in measured and predicted residual stresses cannot be attributed to material variability.

The monotonic stress versus strain properties were used for all Neuber's Rule calculations. It was assumed that no reverse plasticity occurred on unloading. However, AISI 4340 steel exhibits significant cyclic softening [56]. Accounting for reverse plasticity would reduce the magnitude of the predictions as shown in Figure (25).

Independent calculations on this data using the properties of a similar steel and accounting for reverse plasticity showed excellent agreement with the measured results [60].

5.6 Stress Corrosion Cracking/Hydrogen Embrittlement Tests

The results of the SCC/HE tests are given in Table (8) and shown in Figure (26). Time to failure is plotted as a function of applied stress for the cylindrical specimens and is compared with notch stress for the notched specimens. The relationship between stress and time to failure is essentially linear for both the cylindrical and notched specimens. Linear regression performed on both data sets resulted in a slope of -2.71 for the cylindrical specimens and -2.02 for the notched specimens. Although the data are limited for the cylindrical specimens, the results indicate that the slopes of the stress vs. time to failure curves for both specimen types are very close. However, the figure shows that the cylindrical specimens failed at significantly shorter times than did the notched specimens for a given stress level.

Data for the notched specimens were also corrected for residual stress by adding the maximum of the residual stresses measured in the notches to the applied notch

stress:

$$\sigma_C = \sigma_A + \sigma_{RS} \qquad (8)$$

where,

σ_C = corrected notch stress

σ_A = applied notch stress ($k_t S$)

σ_{RS} = maximum measured residual stress

It should be noted that this equation is valid only for $\sigma_C < \sigma_Y$. During the experiments done here, all σ_C values were held below σ_Y. The results plotted in Figure (27) show no effect of residual stresses on the time to failure of the notched specimens. In fact, the applied stress data for specimens containing tensile and those containing compressive residual stresses falls on the curve for the nominally zero residual stress specimens.

Table (8). Stress versus time to failure for SCC/HE tests of AISI 4340 steel.

SPEC. ID	TIME TO FAILURE (min.)	NET SECT NOMINAL STRESS (ksi)	NOTCH STRESS (k_t*S) (ksi)	RESIDUAL STRESS SIDE 1 (ksi)	RESIDUAL STRESS SIDE 2 (ksi)	MAX. CORRECTED STRESS (ksi)
RH-1	33	78.65	158.87	-64.7	-76.4	94.2
RH-2	46	71.50	144.43	-77.7	-74.7	69.7
RH-3	63	42.90	86.66	39.0	78.3	165.0
RH-4	79	42.90	86.66	19.3	21.6	108.3
RH-8	55	60.78	122.77	-6.6	0.9	123.7
RH-10	63	42.90	86.66	-8.8	-19.7	77.9
RH-13	40	78.65	158.87	9.1	-17.8	168.0
RH-14	30	100.10	171.00	-16.1	-1.2	169.8
RHT-1	3	58.87	----	-----		58.9
RHT-2	28	86.66	----	-----		86.7
RHT-3	10	122.77	----	-----		122.8

6.0 DISCUSSION

The previous section showed no correlation was found between surface residual stress and the SCC/HE behavior of AISI 4340 steel in these experiments. It is possible that there is no effect for this alloy/environment system. However, the evidence in the literature [7,10-13] suggests that residual stress should play a role in SCC/HE behavior. Why, then, was this series of experiments unable to measure an effect?

6.1 Total Time to Failure Criterion

The specimen life or total time to failure can be broken into crack initiation and crack growth phases. If crack initiation occurred at the specimen surface, residual stresses would be expected to effect the time to crack initiation. Varying hydrogen concentrations, and therefore varying test times, would be required to initiate a crack depending on the sum of the applied and residual stresses, Figure (28). However, if crack initiation occurred in the interior of the specimen and the residual stress gradient was fairly steep, surface residual stresses would not be expected to play a role in the time to crack initiation. The critical hydrogen concentration would be a function only of the applied stress, Figure (29).

An additional weakness in the use of the total time to failure criterion in observing this phenomenon is that it includes both crack initiation and crack growth time. The ratio of time to crack initiation to crack growth time may vary with applied stress in load-controlled tests. If the time to crack initiation is a large percentage of the total time to failure, (as may be the case in the high applied stress) this criterion can be sensitive to the effects of surface residual stresses. If the time to crack initiation

is an insignificant portion of the total time to failure, (as may be the case in the low applied stress) this criterion is insensitive to surface residual stress effects. The data for the cylindrical specimens relative to that of the notched specimens, Figure (26), indicate that crack initiation occurs fairly early in the total life of the specimens. The cracks grow more slowly in the notched specimens since they are growing into a decaying stress field away from the notch while the cylindrical specimens are growing into a constant stress field, Figure (30). This result indicates that the total time to failure criterion is insensitive for this alloy and electrolyte system.

6.2 Aggressiveness of Electrolyte

AISI 4340 steel has been shown to be extremely susceptible to SCC/HE cracking in 3.5% NaCl solutions [61,62]. This environment was made more damaging by the increased acidification, the use of the Na_2S hydrogen recombination poison, and the -0.7 V applied potential. Further, all oxides were removed immediately prior to testing with the 10% HCl solution. All of these factors make the ingress of hydrogen into the lattice more

favorable. The potential acts to provide large amounts of hydrogen at the specimen surface by the chemical reduction of water. It has been demonstrated that overpotentials as small as 1.1 V in 0.1 N NaOH electrolyte are equivalent to one atmosphere of hydrogen gas [63]. The Na_2S acts to prevent the H^+ ions which have adsorbed onto the specimen surface from recombining with other adsorbed H^+ ions and bubbling off. Treatment of the specimen surfaces with 10% HCl just prior to testing activated the surfaces and removed any barriers to diffusion which might have existed in the form of oxides.

With all of these factors acting to promote the absorption of hydrogen into the lattice, and due to the susceptibility of the alloy to SCC/HE cracking, it is highly possible that crack initiation occurred very shortly after exposure. Relatively short times would be necessary to accumulate the required H^+ concentration at the specimen surface for crack initiation even in the cases of the specimens with the compressive residual stresses. After crack initiation, the stress relieved specimens and the specimens containing residual stresses would have similar times to failure since most of the specimen life would be taken up in crack growth.

7.0 CONCLUSIONS

The objective of the work described here was to evaluate the effect of surface residual stresses on the SCC/HE behavior of AISI 4340 steel. For reasons described above, no effect of surface residual stress on SCC/HE behavior was detected. However, the results of this work lead to the following conclusions:

a) AISI 4340 steel with a tempered martensitic microstructure was found to exhibit interlath or intergranular SCC/HE cracking in acidified 3.5% NaCl solution;

b) Surface residual stresses were readily measured in AISI 4340 steel using an X-ray technique;

c) Neuber's rule estimates of residual stresses were larger in magnitude than those measured using x-rays when no reverse plasticity was assumed. Accounting for reverse plasticity using real stress versus strain behavior would bring the predicted and measured residual stresses into good agreement;

d) The total time to failure criterion was not sufficiently sensitive to evaluate the effect of residual

stresses on the SCC/HE behavior of notched AISI 4340 steel specimens;

e) Residual stresses did not act to increase or decrease the total specimen life under SCC/HE conditions for this material, environment, and specimen geometry.

8.0 RECOMMENDATIONS FOR FUTURE WORK

Based on the findings of the work described here, some additional research should be done in order to properly evaluate the effects of residual stresses on the SCC/HE behavior of AISI 4340 steel. Recommendations for this work are given below.

1) Specimens should have a simple stress profile, ie., cylindrical tensile specimens or four-point bend specimens. This would eliminate the complication of the combined applied and residual stress gradients.

2) Methodologies for detection of crack initiation should be more actively pursued. Acoustic emission has been shown to be a viable technique in detecting SCC/HE [64-67]. Refinement of the techniques for this application is required. Strain gaging in the test section is an additional technique that may be simple and effective in

determining crack initiation.

3) A less aggressive environment should be used in order to lengthen the time to crack initiation and ultimate failure and increase the resolution of the data. It is always more desirable to perform tests in the service environment.

4) After determination of the time to failure at a given stress, a series of specimens should be tested at various fractions of this time. The specimens should then be metallographically sectioned in an attempt to determine whether crack initiation occurs on the surface or the interior of the specimen.

5) In order to more fully understand the tests run during this investigation, the stress profile across the specimen face should be measured. Knowledge of the depth of the residual stress zone resulting from plasticity at the notch root is critical in understanding these results.

REFERENCES

1. "Practices for Detecting Susceptibility to Intergranular Attack in Austenitic Stainless Steels", ASTM Standard A 262 - 86, American Society for Testing and Materials, Philadelphia, 1986.

2. "Recommended Practice for Detection of Susceptibility to Intergranular Corrosion in Severly Sensitized Austenitic Stainless Steel", ASTM Standard A 708 - 79, American Society for Testing and Materials, Philadelphia, 1979.

3. "Test Methods of Detecting Susceptibility to Intergranular Attack in Wrought, Nickel-Rich, Chromium-Bearing Alloys, ASTM Standard G 28 - 85, American Society for Testing and Materials, Philadelphia, 1985.

4. "Practice for Making and Using U-Bend Stress-Corrosion Test Specimens", ASTM Standard G 30 - 79, revised 1984, American Society for Testing and Materials, Philadelphia, 1984.

5. "Practice for Determining the Susceptibility of Stainless Steels and Related Nickel-Chromium-Iron Alloys to Stress-Corrosion Cracking in Polythionic Acids, ASTM Standard G 35 - 73, revised 1982, American Society for

Testing and Materials, Philadelphia, 1982.

6. NACE Standard MR-01-75, National Association of Corrosion Engineers, Houston, 1980.

7. Staehle, R.W., "Comments on the History, Engineering and Science of Stress Corrosion Cracking", proceedings of conference "Fundamental Aspects of Stress Corrosion Cracking", Ohio State University, Sep., 1967.

8. Kruger, J., "Failure by Stress Corrosion Cracking - Current Approaches Toward Failure Prediction", Stress Corrosion Cracking, J. Yahalom and A. Aladjem eds., Freund Publishing House, Tel-Aviv, Israel, 1980.

9. Brown, B.F., Naval Research Laboratory Report 7130, June 1970.

10. National Materials Advisory Board, "Characterization of Environmentally Assisted Cracking for Design: State of the Art", U.S. Nuclear Regulatory Commission, NMAB-386, 1982.

11. Shack, W.J., Kassner, T.F., Maiya, P.S., Nichols, F.A., and Park, J.Y., "Evaluation of Stainless Steel Pipe Cracking: Causes and Fixes", U.S. Department of Energy, CONF-8310143-60, Oct. 1983.

12. Jenkins, C.F., "Surface Stress Modification for Repair of Stress-Relieved Carbon Steel Fabrications", proceedings of 1985 International Conference on Surface Modification and Coatings, ASM, Toronto, 1985.

13. Kohls, J.B., Cammett, J.T., and Gunderson, A.W., "Effects of Multiple Shot-Peening/Cadmium-Plating Cycles on High-Strength Steel", ASTM STP 776, pp. 158-171, 1982.

14. B.F. Brown, "Stress-Corrosion Cracking in High Strength Steels and in Titanium and Aluminum Alloys", B.F. Brown ed., Naval Research Laboratory, U.S. Gov't Printing Office, Washington, D.C., 1972.

15. Uhlig, H.H., and Cook, E., J. Electrochem. Soc. 116:173, 1969.

16. Chu, W. -Y., Yao, J., and Hsiao C. -M., Corrosion, Vol. 40 8:302-306, 1984.

17. Chu, W. -Y., Ma, R. -T., and Hsiao, C. -M., Corrosion, Vol. 43 4:251-254, 1987.

18. Takemoto, M., Corrosion, Vol. 42, No. 10, pp. 585-592, 1986.

19. Shively, J.H., Hehemann, R.F., and Troiano, Corrosion, 22:253, 1966.

20. Ford, F.P., "Stress Corrosion Cracking of Iron-Base Alloys in Aqueous Environments", Treatise on Materials Science and Technology, Vol. 25, pp 235-269, 1983.

21. Kortovich, C.S., and Steigerwald, F.A., Eng. Fracture Mech., Vol. 4 pp 637-651, 1972.

22. Marichev, Y.A. and Rosenfeld, I.L., Corrosion, Vol. 32 No. 11, pp. 423-429, 1976.

23. Zapffe, C. and Sims, C., Trans AIME 145:225-59, 1941.

24. de Kazinsky, F.J., J. Iron and Steel Inst. 177:85-92, 1954.

25. Tetelman, A.S., and Robertson, W.D. Acta Metallurgica 11:415-26, 1963.

26. Oriani, R.A., Ann. Rev. of Mater. Sci. 8:327-57, 1978.

27. Petch, N.J., Philos. Mag. 1 (Ser. 8):331-337.

28. Oriani, R.A. and Josephic, P.H., Acta Metallurgica 22:1065-74, 1974.

29. Uhlig, H.H., Fundamental Aspects of Stress Corrosion

Cracking, p 86, R.W. Staehle, A.J. Forty, and D. Van Rooyan eds., NACE, Houston, 1969.

30. Logan, H.L., J. Res. Natl. Bur. of Stds, 48:99, 1952.

31. Champion, F.A., "International Symposium on Stress in Metals and Alloys", Institute of Metals, London, p. 468, 1948.

32. Beachem, C.D., Met. Trans., 3:437-51.

33. Thompson, A.W. and Bernstein, I.M., "Advances in Corrosion Science and Technology", Plenum Press, New York, 1978.

34. McBreen, J. and Gneshaw, M.A., "The Electrolytic Introduction of Hydrogen into Metals", Fundamental Aspects of Stress Corrosion Cracking, p. 51, R.W. Staehle, A.J. Forty, and D. Van Rooyan, eds., NACE, Houston, 1969.

35. Bernstein, I.M., and Thompson, A.W., "An Evaluation of Hydrogen Embrittlement Mechanisms", Mechanisms of Environment Sensitive Cracking of Materials, Swann, P.R., Ford, F.P., and Westwood, A.R.C., eds., The Metals Society, London, 1977.

36. Oriani, R.A., "Hydrogen in Metals", Fundamental

Aspects of Stress Corrosion Cracking, p. 32, R.W. Staehle, A.J. Forty, and D. Van Rooyan, eds., NACE, Houston, 1969.

37. McBreen, J., Nanis, L., and Beck, W., J. Electrochem. Soc., pp. 1218-1221, Nov., 1966.

38. Bernstein, I.M., Garber, R., and Pressouyre, G.M., Effect of Hydrogen on Behavior of Materials, A.W. Thompson and I.M. Bernstein, eds., p. 37, TMS-AIME, New York, 1976.

39. Darken, L.S. and Smith, R.P., Corrosion, Vol. 5, p. 1, 1949.

40. Pressouyre, G.M. and Bernstein, I.M., Met. Trans. A, Vol. 9A pp. 1571-1579, Nov., 1978.

41. Johnson, E.W., and Hill, M.L., Trans. Met. Soc., AIME, 218, 1104, 1960.

42. Naeser, G. and Dautzenberg, Arch. Eisenhuttenw., 36, 173, 1965.

43. Robinson, M.J., and Sharp, R.M., "The Effect of Post-Exposure Heat Treatment on the Hydrogen Embrittlement of High Carbon Steel", Corrosion, NACE, Vol. 41, No. 10, p. 582, 1985.

44. Zakroczymski, T., "An Electrochemical Method for Hydrogen Determination in Steel", Corrosion, NACE, Vol. 38, No. 4, p. 218, 1982.

45. Townsend, H.E., "A Study of the Entry and Removal of Hydrogen During Coating and Thermal Treatment of Steel", Corrosion, NACE, Vol. 37, No. 2, 1981.

46. Li, J.C.M., Oriani, R.A., and Darken, L.S., Z. Physik. Chem., 49, 271, 1966.

47. Whiteman, M.B. and Troiano, A.R., Phys. Stat. Sol., K109, 1964.

48. Berkowitz, B.J. and Horowitz, H.H., "The Role of H_2S in the Corrosion and Hydrogen Embrittlement of Steel", J. Electrochem. Soc. Vol. 129 3:468-474, March, 1982.

49. Venkatasubramanian, T.V. and Baker, T.J., "Role of MnS Inclusions in Hydrogen Assisted Cracking of Steel exposed to H_2S Saturated Salt Solution", Metal Science, Vol. 18, pp. 241-247, May, 1984.

50. Ondrejcin, R.S., Rideout, S.P., and Donovan, J.A., "Control of Stress Corrosion Cracking in Storage Tanks Containing Radioactive Waste", Nuclear Technology, 44, p. 297-306, 1979.

51. Nakagawa, Y., Usami, K., Minato, A., Tamamura, T., Sasaki, R., and Naruse, A., "Effects of Surface Finish on Residual Stress Distribution and Stress Corrosion Cracking Susceptibility of Type 304 Austenitic Stainless Steel in a Boiling $MgCl_2$ Solution", Vol. 2, ICM, Cambridge, England, 1979.

52. Harris, D.O., "Stress Corrosion Crack Growth in the Presence of Residual Stresses" proceedings of 28th Sagamore Army Materials Research Conference, E. Kulh and V. Weiss, eds., Plenum Press, 1982.

53. "Standard Specification for Steel Bars, Alloy, Standard Grade", ASTM A322-87, American Society for Testing and Materials, Philadelphia, 1987.

54. Noyan, I.C. and Cohen, J.B., Residual Stress Measurement by Diffraction and Interpretation, Materials Research and Engineering, Springer-Verlag New York, Inc., 1987.

55. Neuber, H., Theory of Notch Stress: Principles for Exact Calculation of Strength with Reference to Structural Form and Material, 2nd Edition, Springer Publishers, Berlin, 1958.

56. Landgraf, R.W., "The Resistance of Metals to Cyclic Deformation", 72nd Annual Meeting of the American Society for Testing and Materials, 1969.

57. Boardman, B.E., "Crack Initiation Fatigue - Data, Analysis, Trends, and Estimation", Proceedings of the SAE Fatigue Conference P109, Society of Automotive Engineers, Warrendale, PA, 1982.

58. Honeycombe, R.W.K., Steels: Microstructure and Properties, American Society for Metals, Edward Arnold Press, 1982.

59. Personal Communication, N.E. Dowling and R.A. Hays, Dec., 1988.

60. Personal Communication, R.W. Landgraf and R.A. Hays, Dec., 1988.

61. Mears, R.B., Brown, R.H., and Dix, E.H. Jr., Symposium on Stress Corrosion Cracking of Metals, p. 323.

62. Wilde, B.E., Corrosion, Vol. 27, p. 326, 1971.

63. Oriani, R.A. and Josephic, P.H., "Hydrogen-Assisted Crack Initiation in a High-Strength Steel", proceedings of

Environment-Sensitive Fracture of Engineering Materials, Z.A. Foroulis, ed., AIME, 1977.

64. Susetka, S.L., "An Investigation of Hydrogen Embrittlement in 4130 Steel Using Acoustic Emission Techniques", PhD. Thesis, Renssalaer Polytechnic Institute, 1986.

65. Gerberich, W.W. and Hartbower, C.E., "Monitoring Crack Growth of Hydrogen Embrittlement and Stress Corrosion Cracking by Acoustic Emission", proceedings of conference "Fundamental Aspects of Stress Corrosion Cracking", Ohio State University, Sep., 1967.

66. Endo, K., Komai, K., and Fujimoto, T., "Environmentally Enhanced Fatigue Crack Growth of a High-Strength Steel Sensitive to Stress Corrosion Cracking", Bulletin of JSME, Vol. 23, No. 180, 1980.

67. Gerberich, W.W., Jones, R.H., Friesel, M.A., and Nozue, A., "Acoustic Emission Monitoring of Stress Corrosion Cracking", proceedings of Workshop on the Mechanics and Physics of Crack Growth: Application to Life Prediction, 1987.

BLANK PAGE

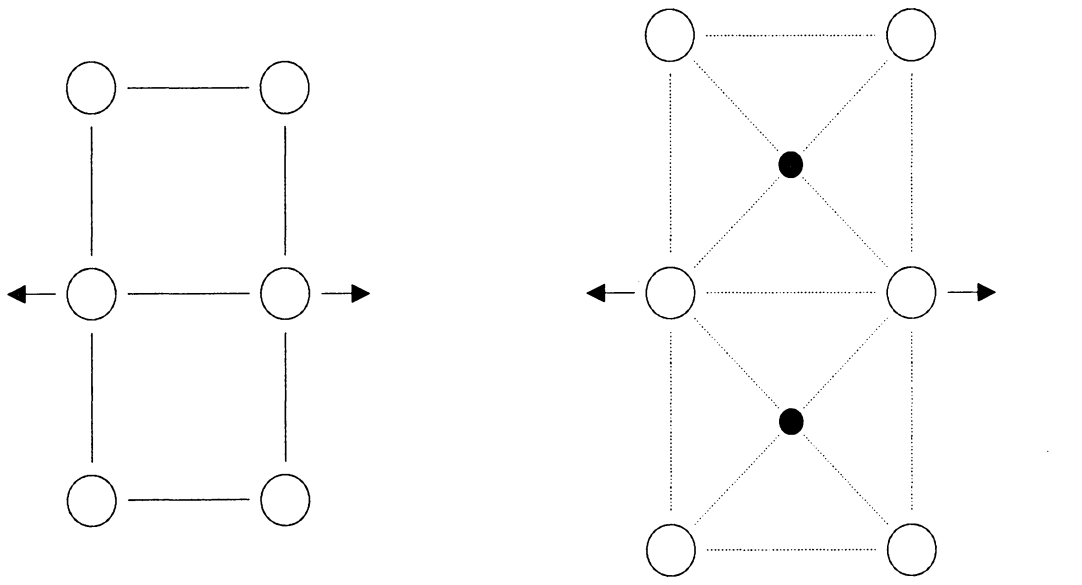

Figure 1. Schematic of reduction in metal/metal bond strength due to hydrogen.

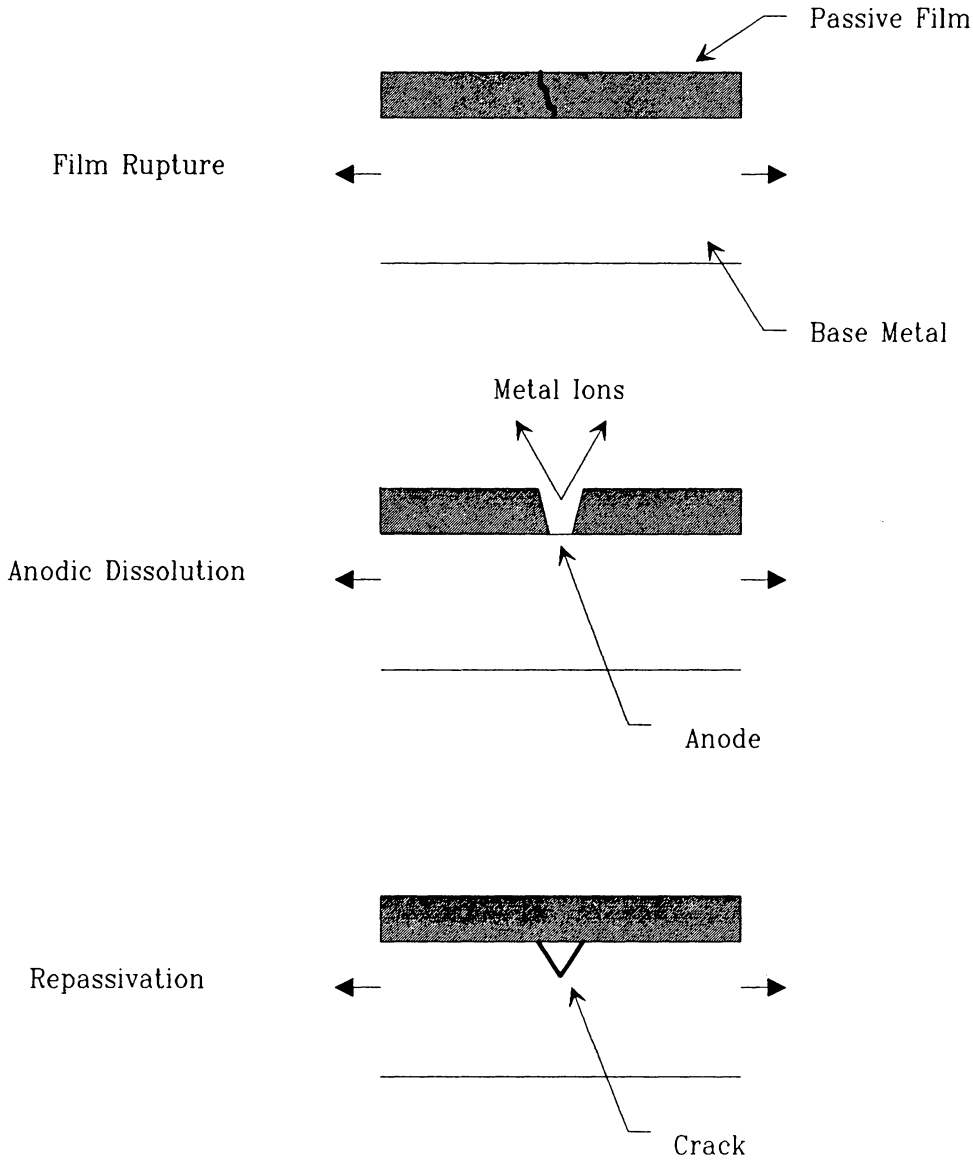

Figure 2. Anodic path dissolution model of SCC/HE.

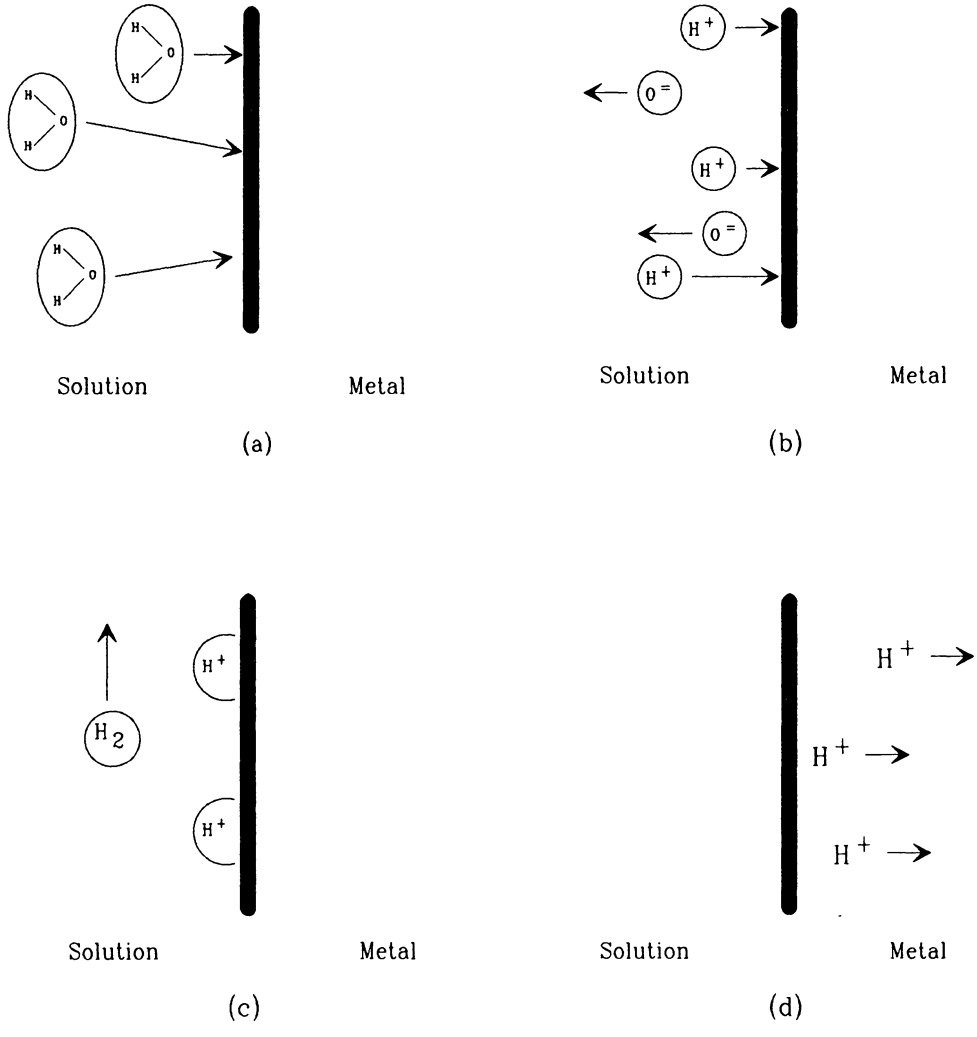

Figure 3. Process of hydrogen entry into metals.

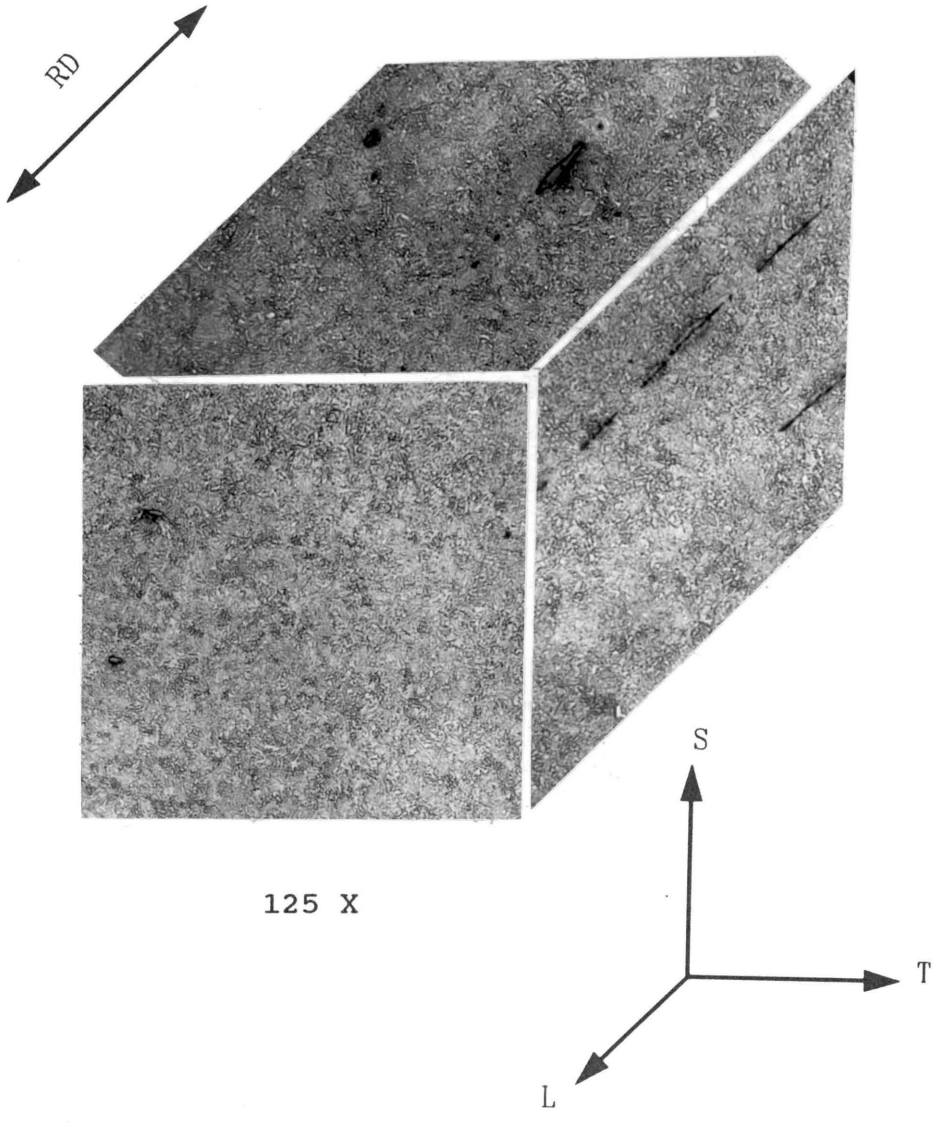

Figure 4. Metallurgical structure of AISI 4340 steel.

650 X

Figure 5. Tempered martensite dominating AISI 4340 steel microstructure.

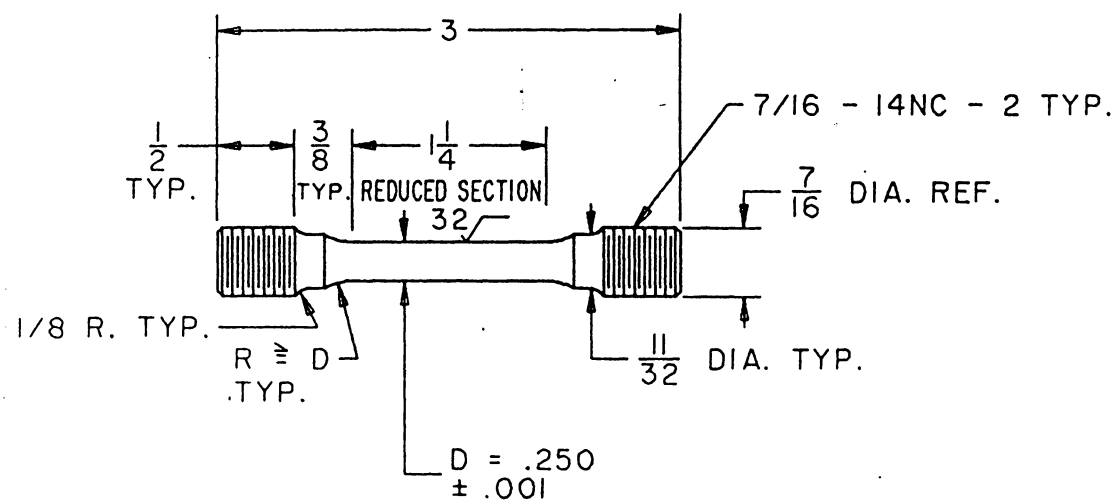

Figure 6. Cylindrical tensile specimen.

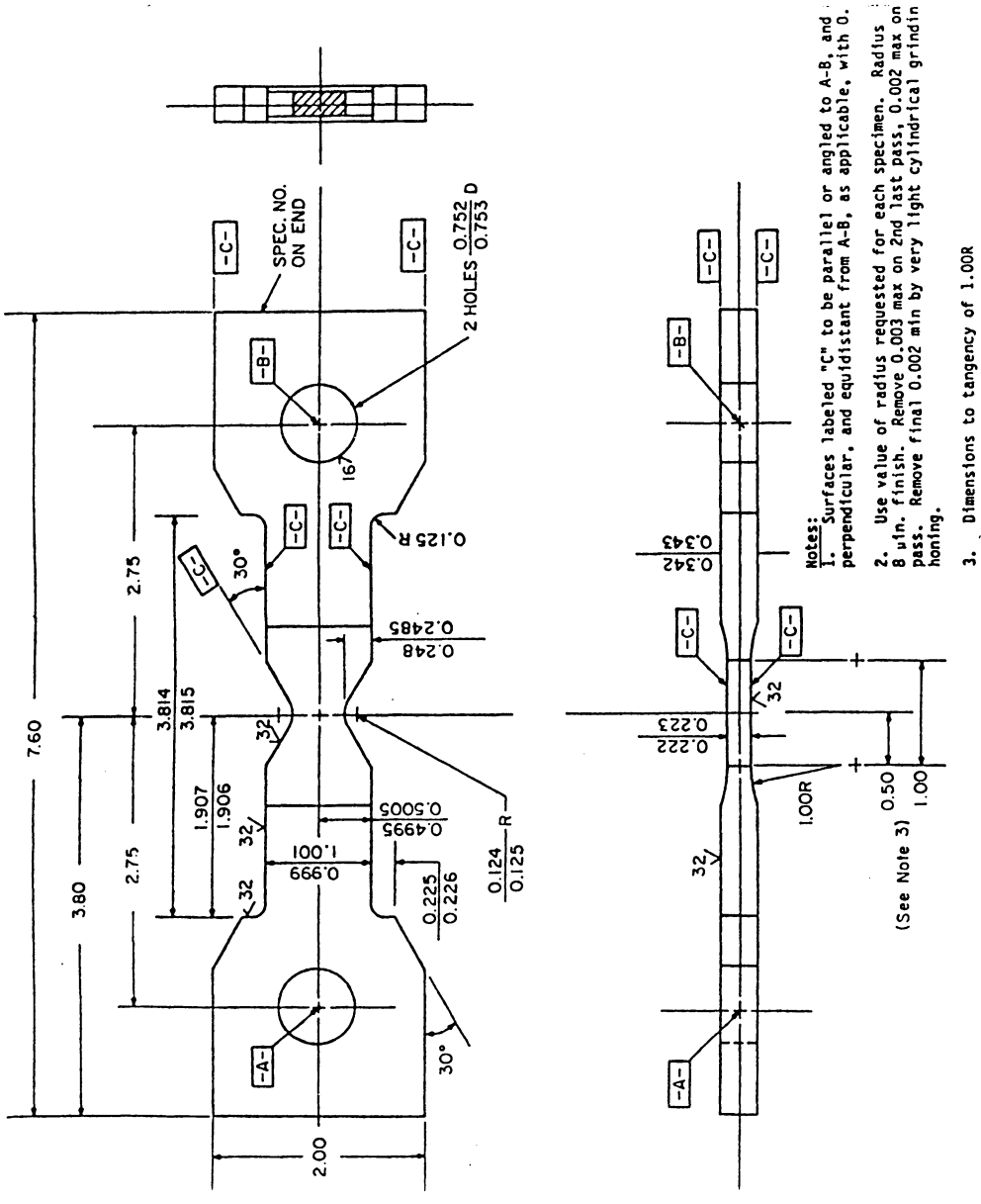

Figure 7. Notched tensile specimen.

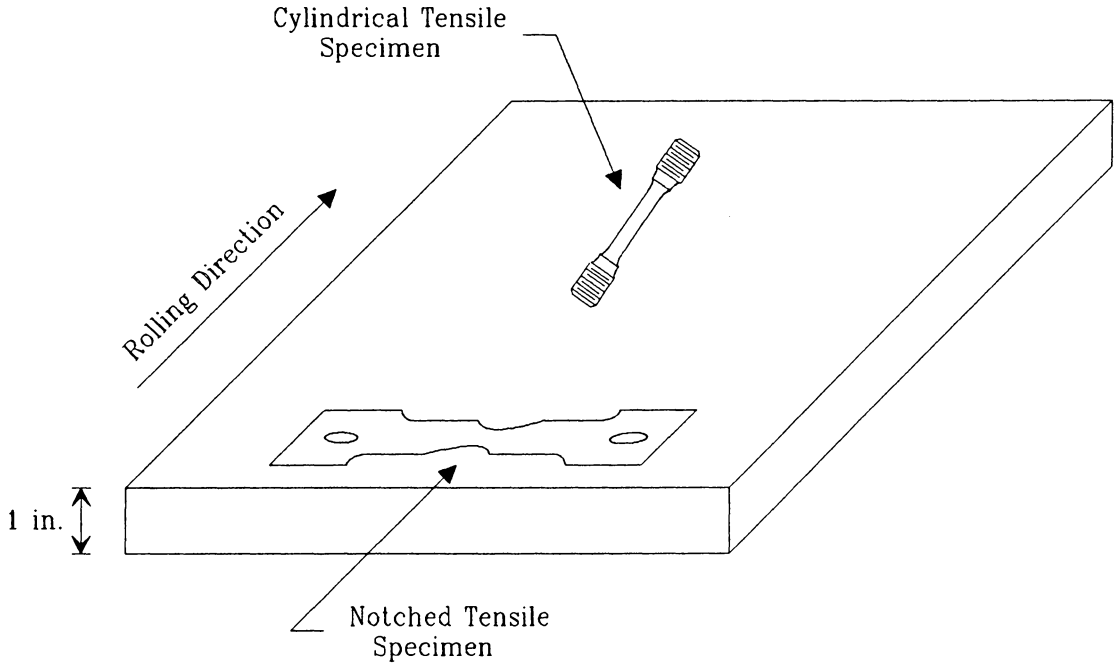

Figure 8. Specimen orientation with respect to plate rolling direction.

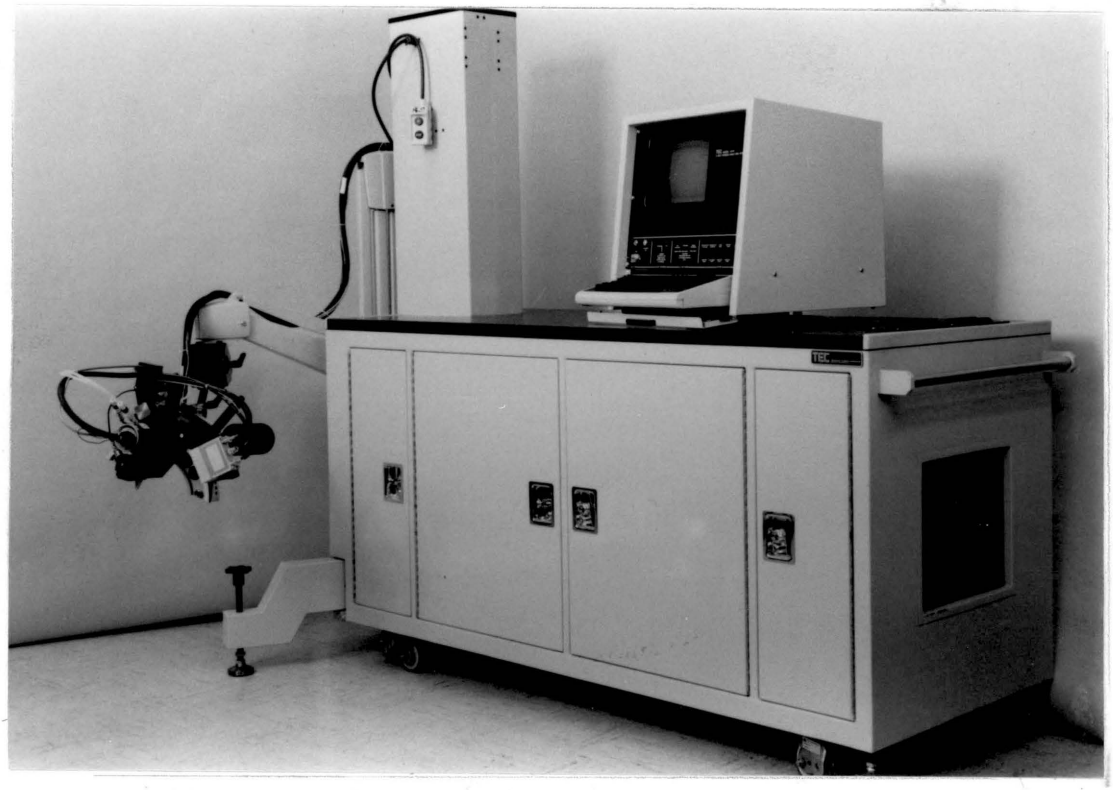

Figure 9. Photograph of X-ray stress analyzer.

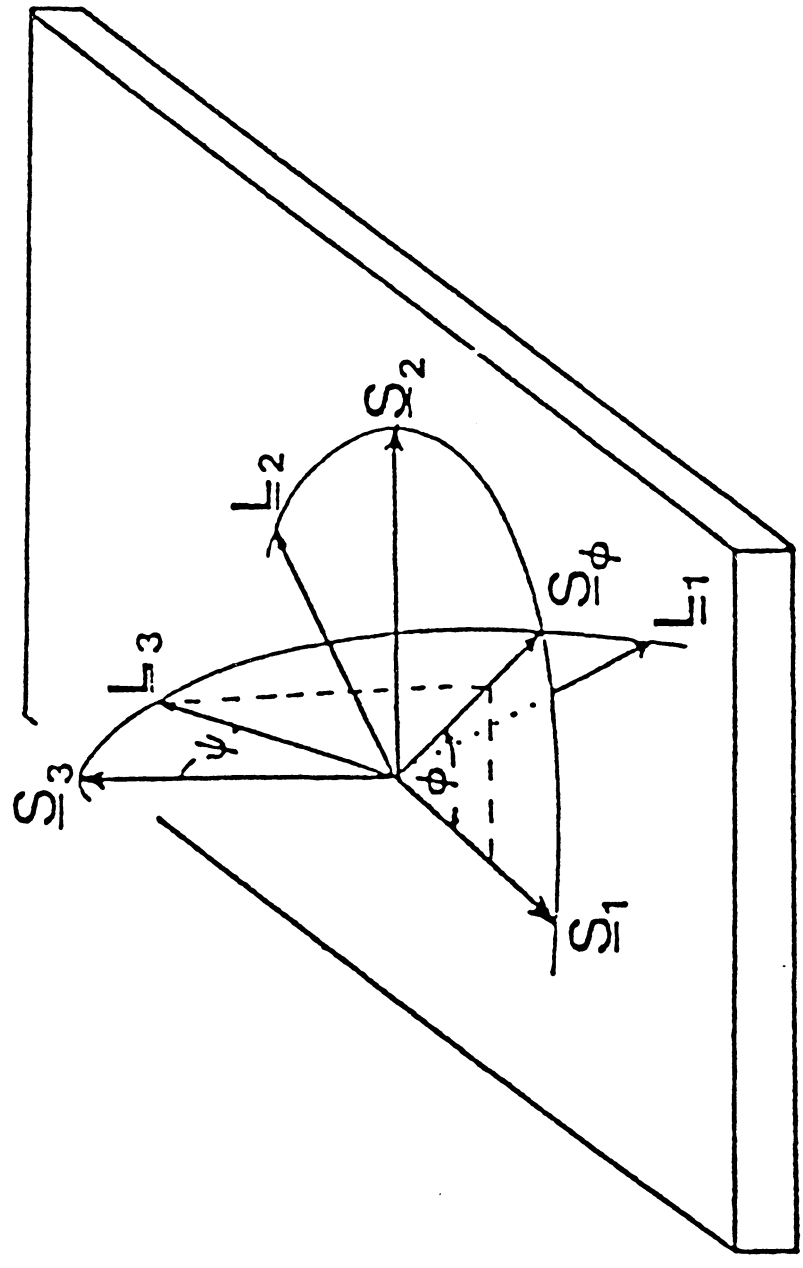

Figure 10. Coordinate system relating stress analyzer and specimens.

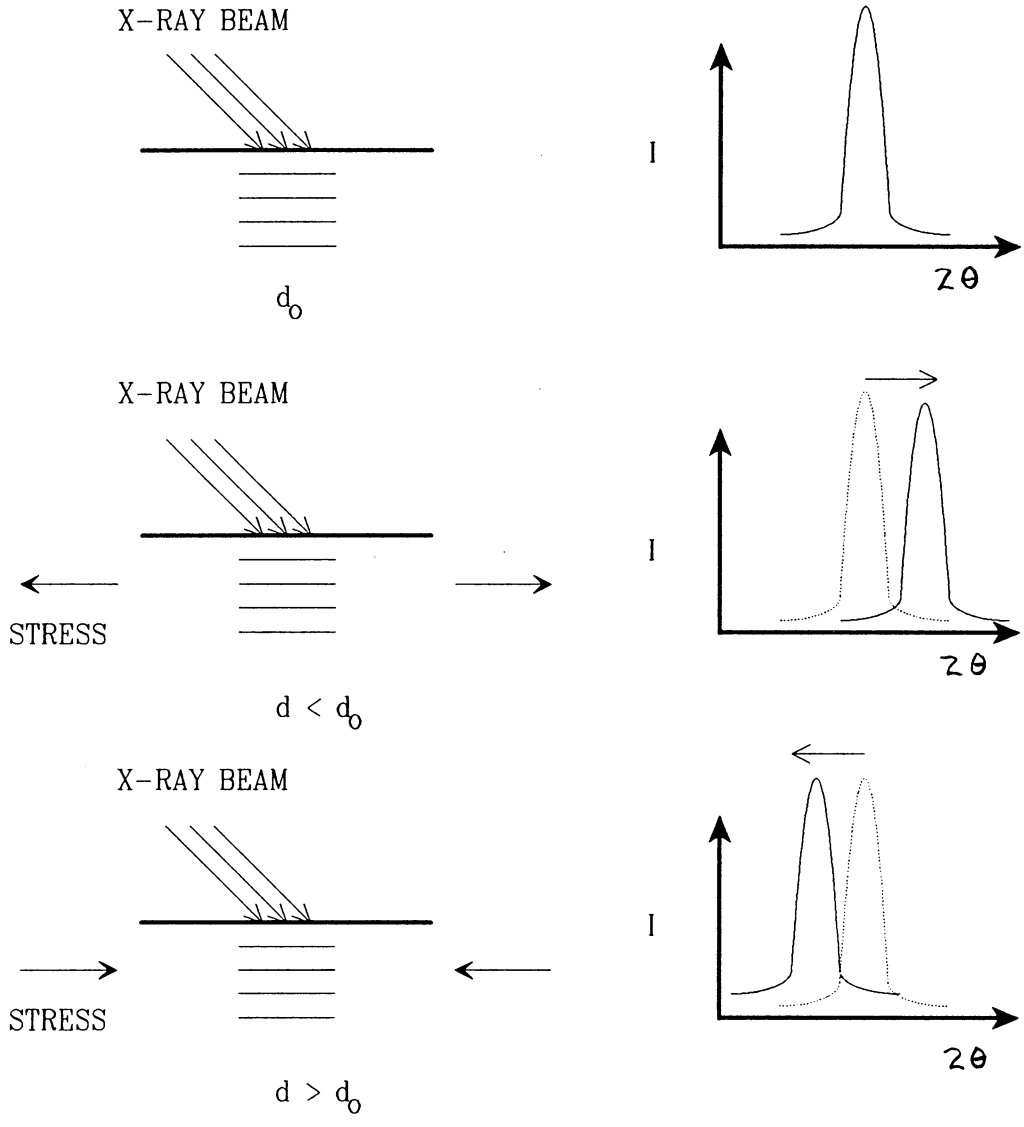

Figure 11. Schematic showing d-spacing variation as a function of orientation with respect to stress axis.

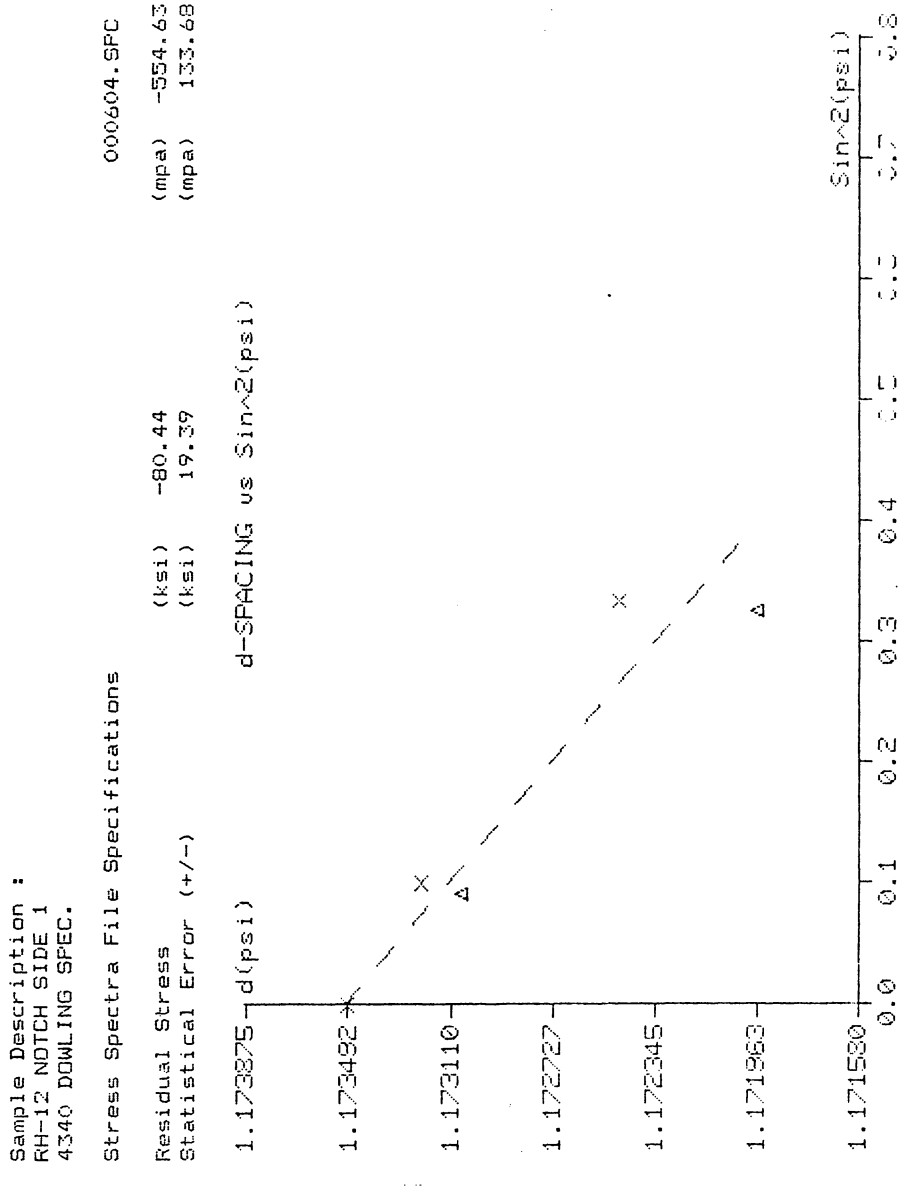

Figure 12. Typical d versus $\sin^2\Psi$ plot from TEC Model 1610 stress analyzer.

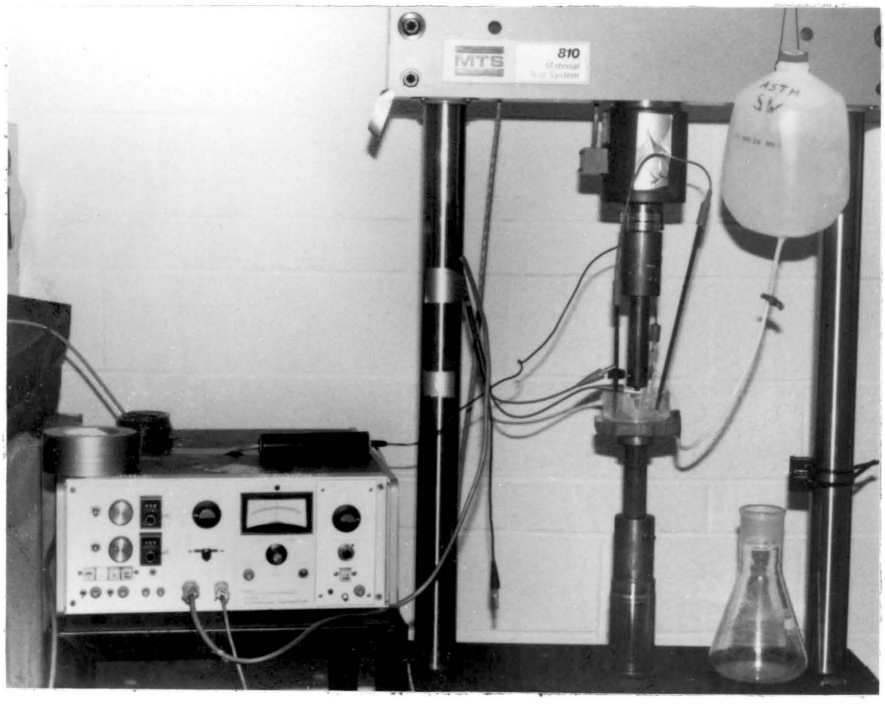

Figure 13. Photograph of cylindrical tensile specimen SCC/HE test.

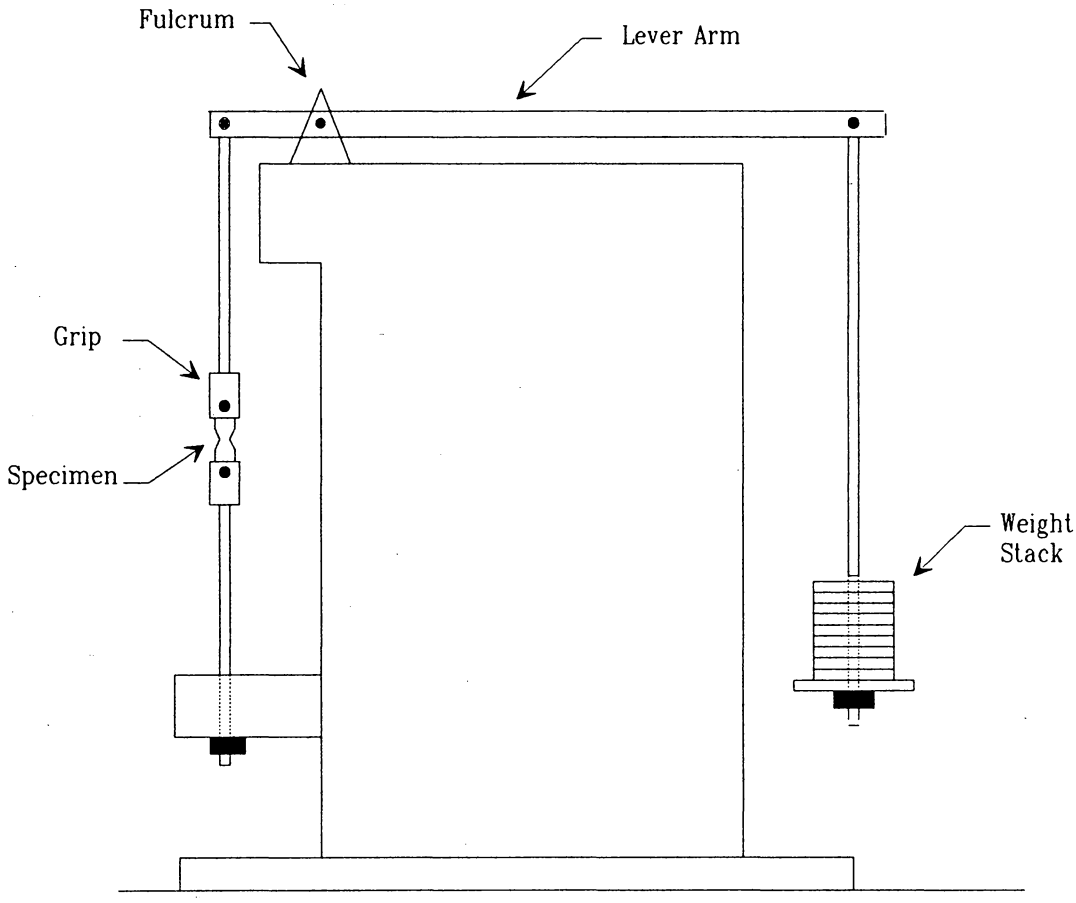

Figure 14. Schematic of notched tensile specimen SCC/HE loading configuration.

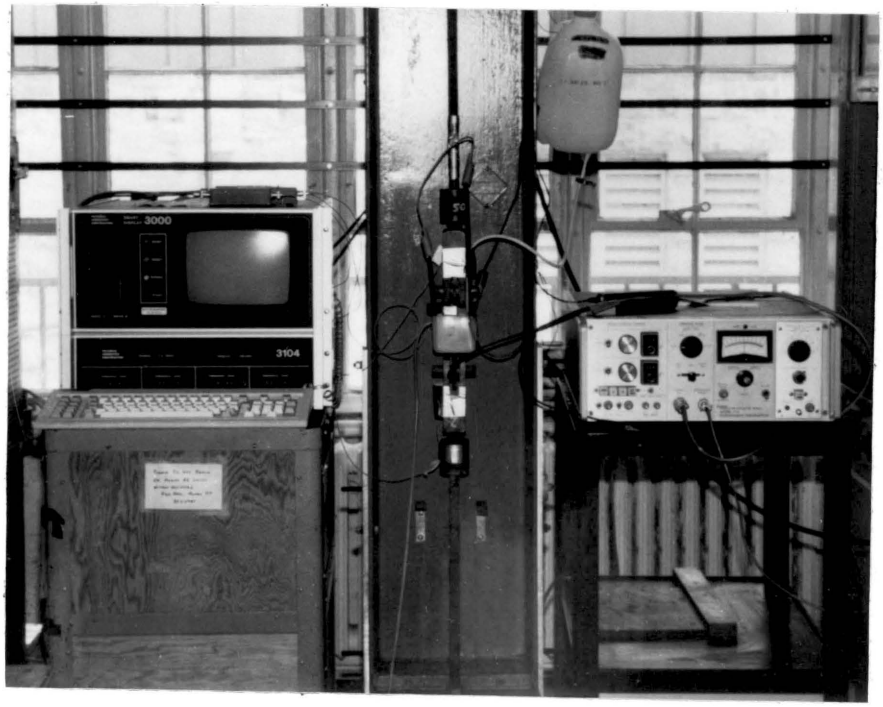

Figure 15. Overview photograph of notched tensile specimen SCC/HE test.

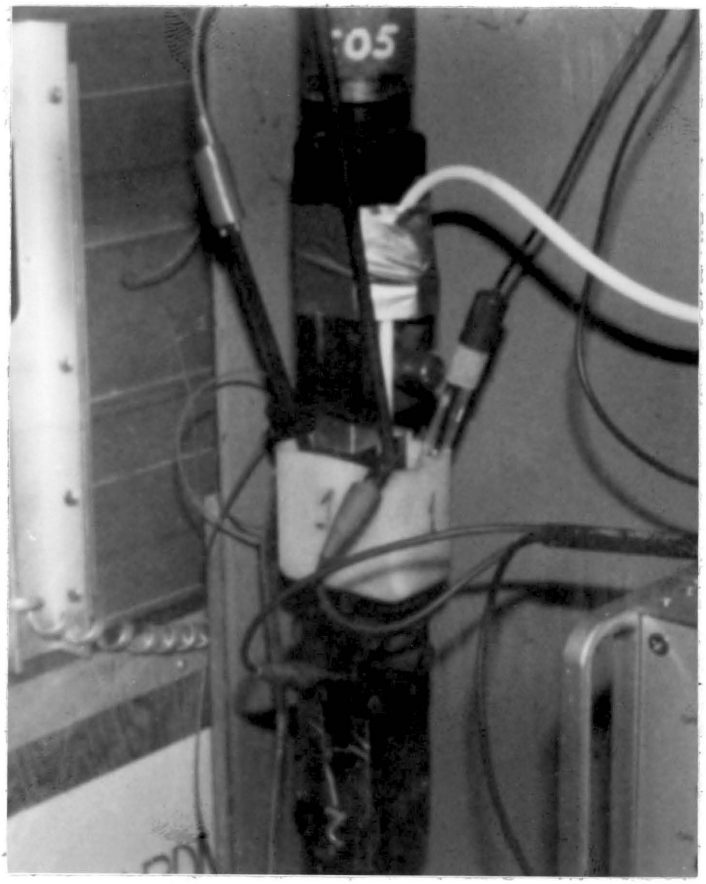

Figure 16. Close up of notched tensile specimen SCC/HE test.

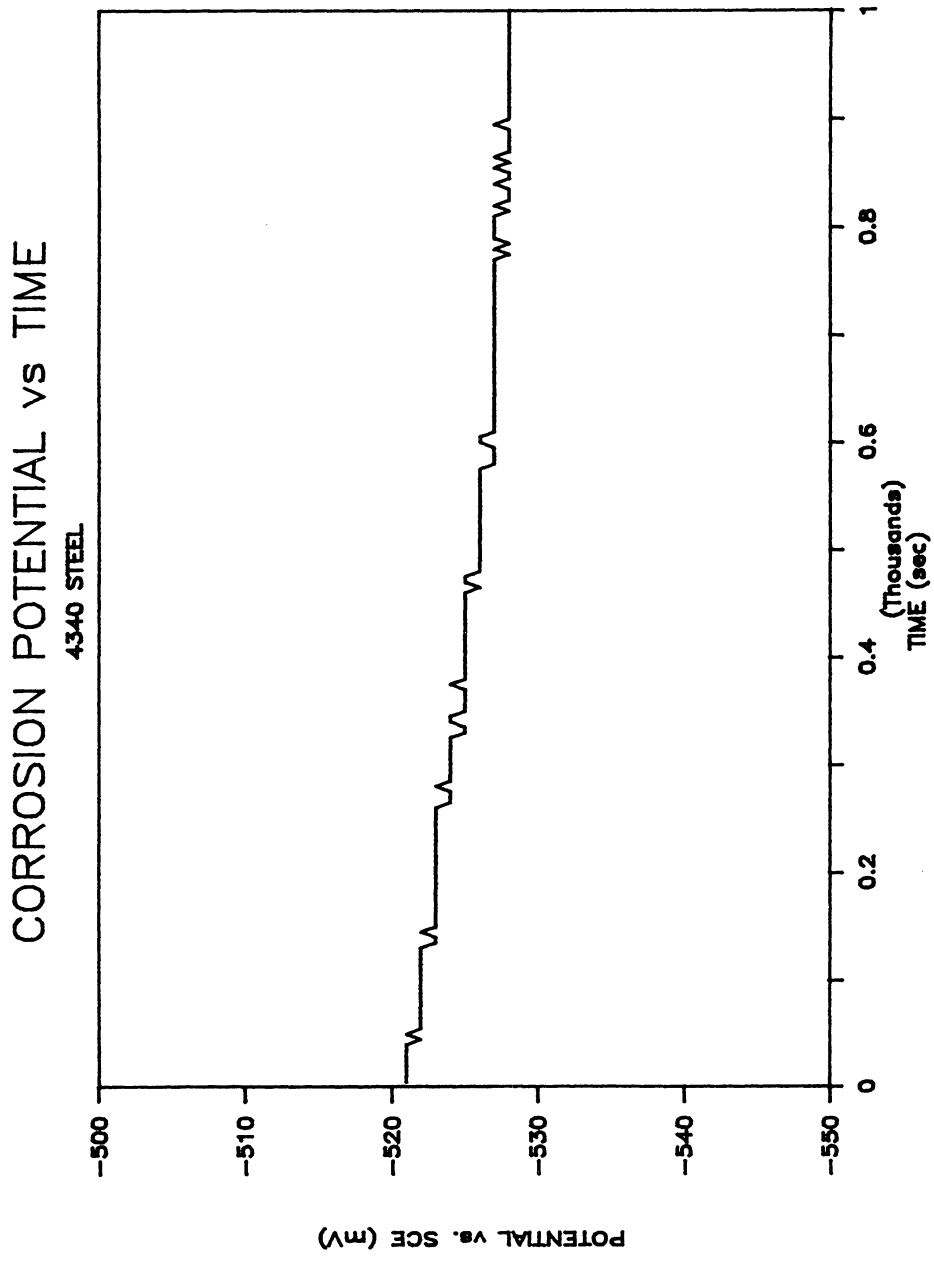

Figure 17. Results of potentiostatic test on AISI 4340 steel.

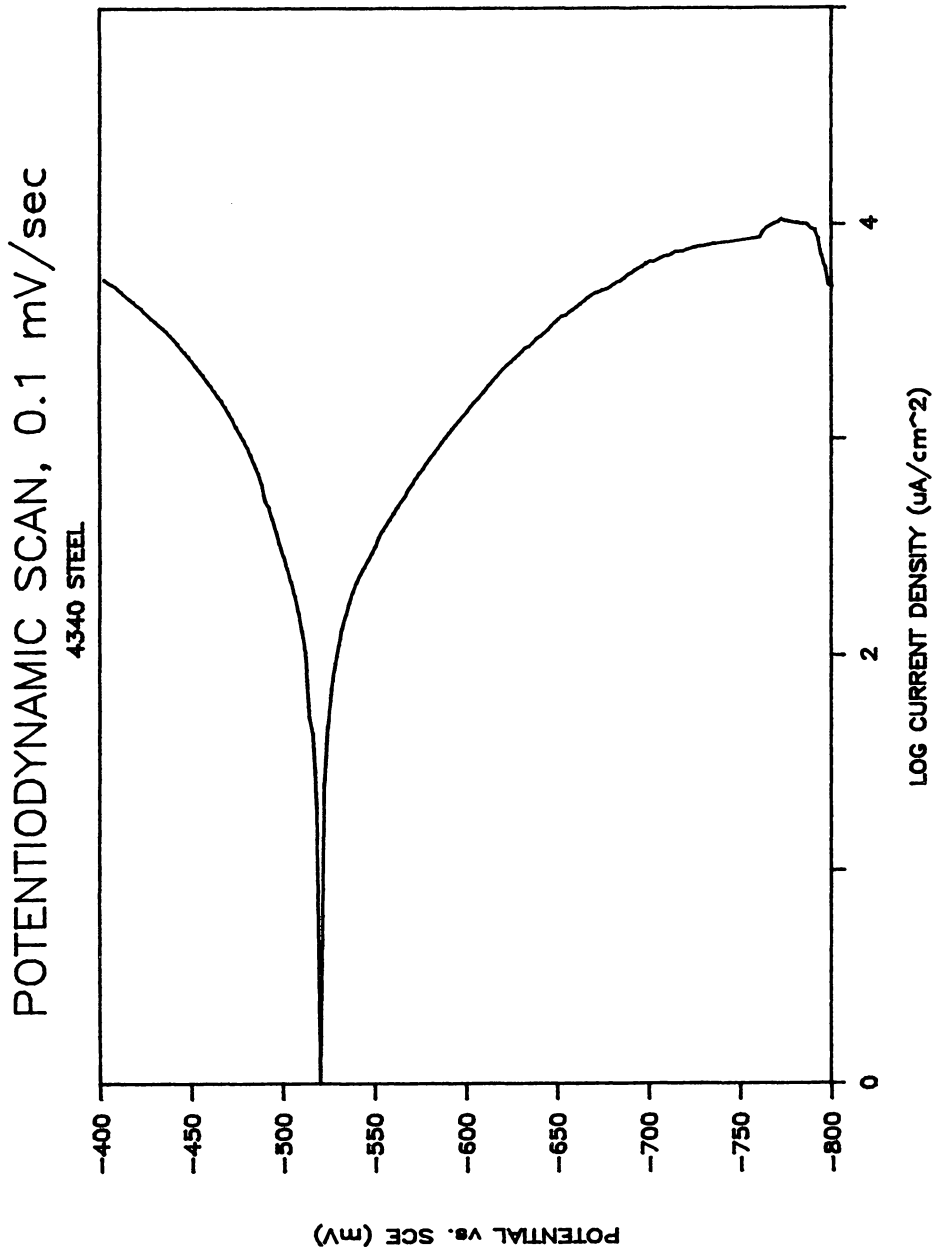

Figure 18. Results of potentiodynamic scan of AISI 4340 steel.

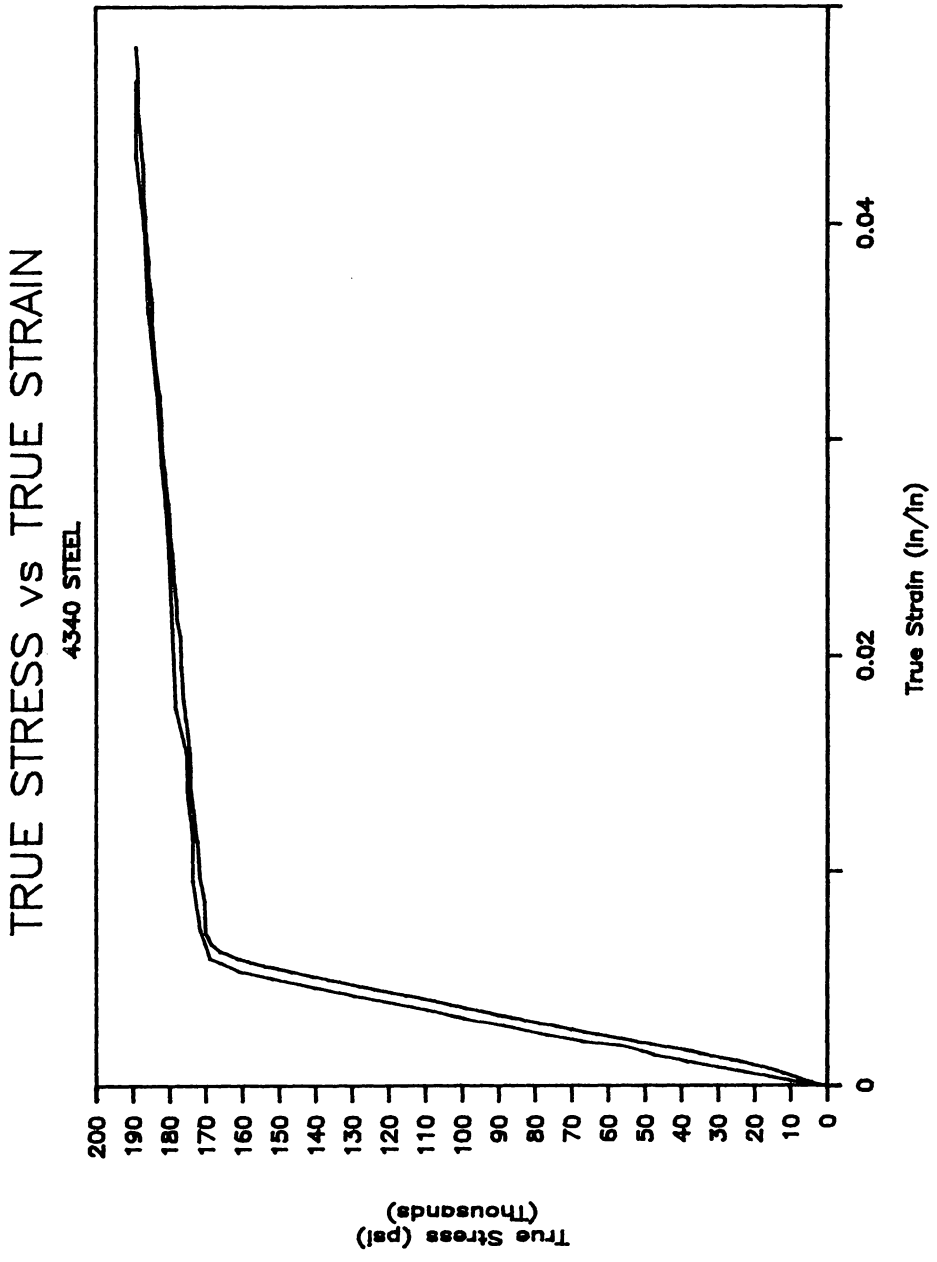

Figure 19. Stress versus strain curve for cylindrical tensile specimens of AISI 4340 steel.

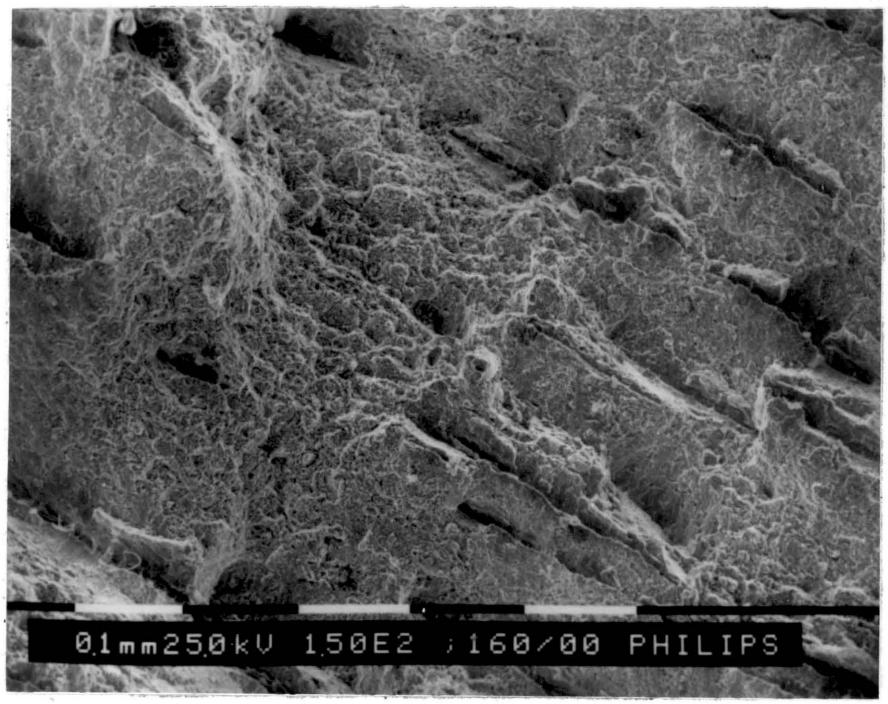

Figure 20. Scanning electron micrograph showing ductile overload failure in cylindrical tensile specimens.

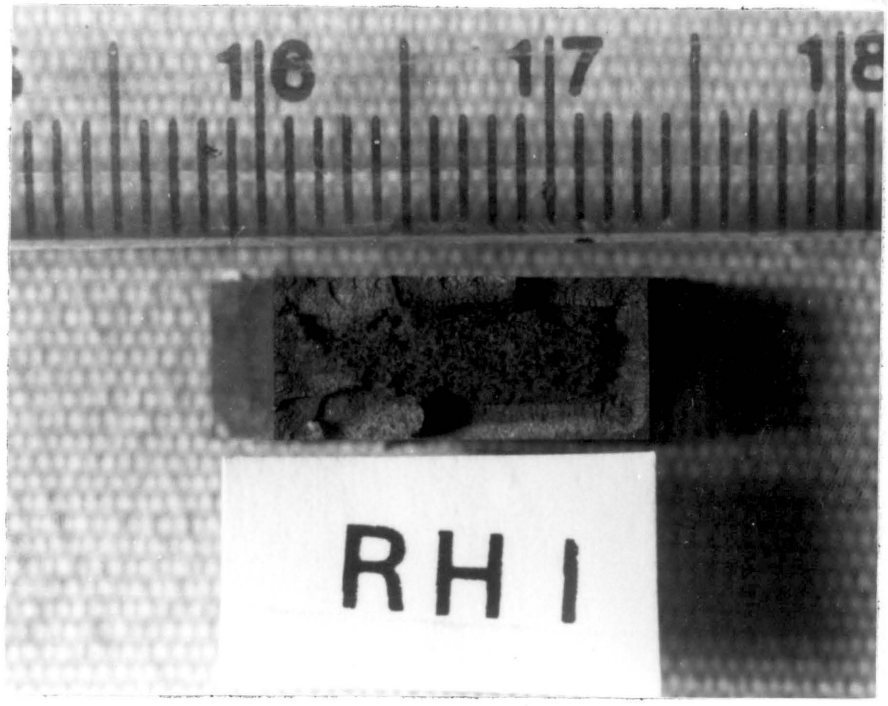

Figure 21. Photograph of interlath or intergranular and fibrous fracture areas on SCC/HE specimens.

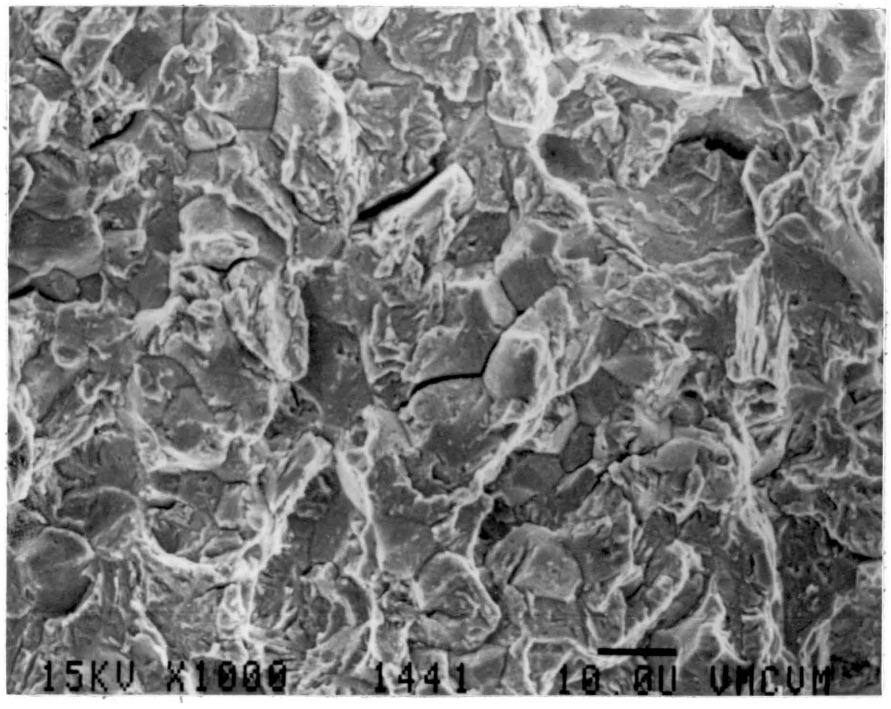

Figure 22. Scanning electron micrograph of interlath or intergranular fracture on SCC/HE specimen.

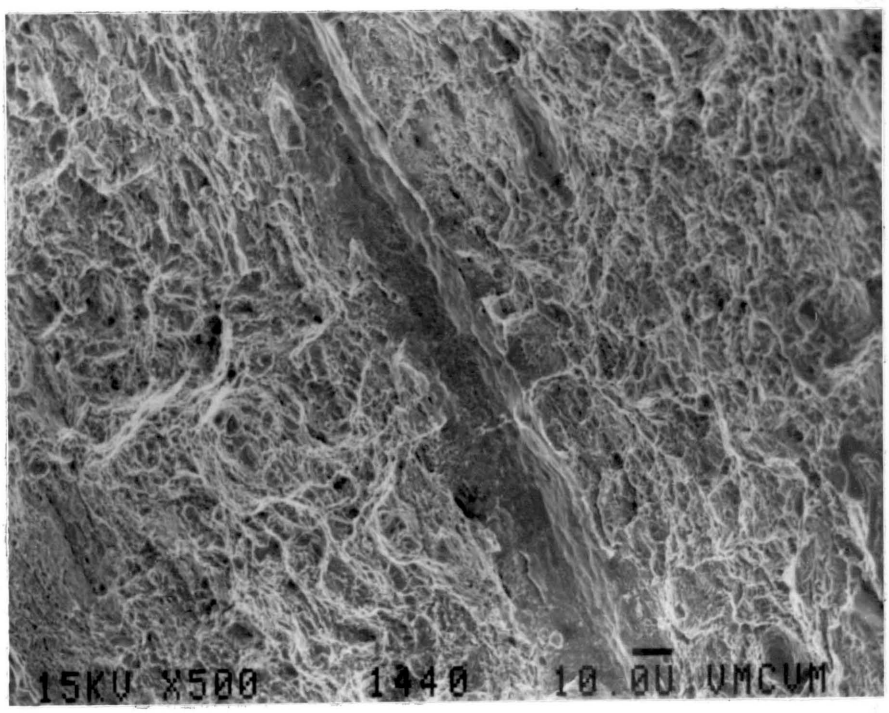

Figure 23. Scanning electron micrograph of fibrous fracture zone in center of specimens.

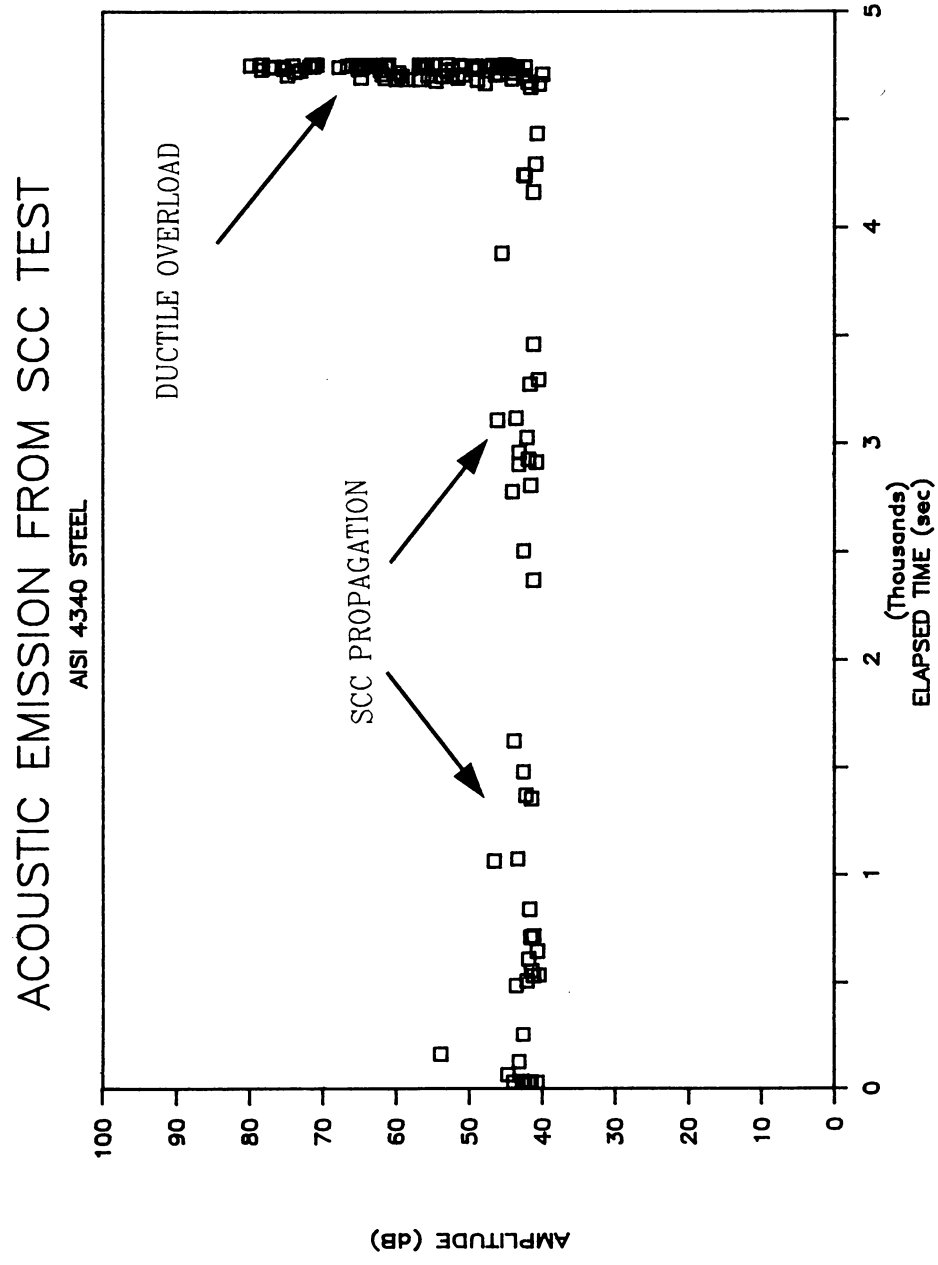

Figure 24. Peak amplitude of acoustic emission versus time for specimen RH-4.

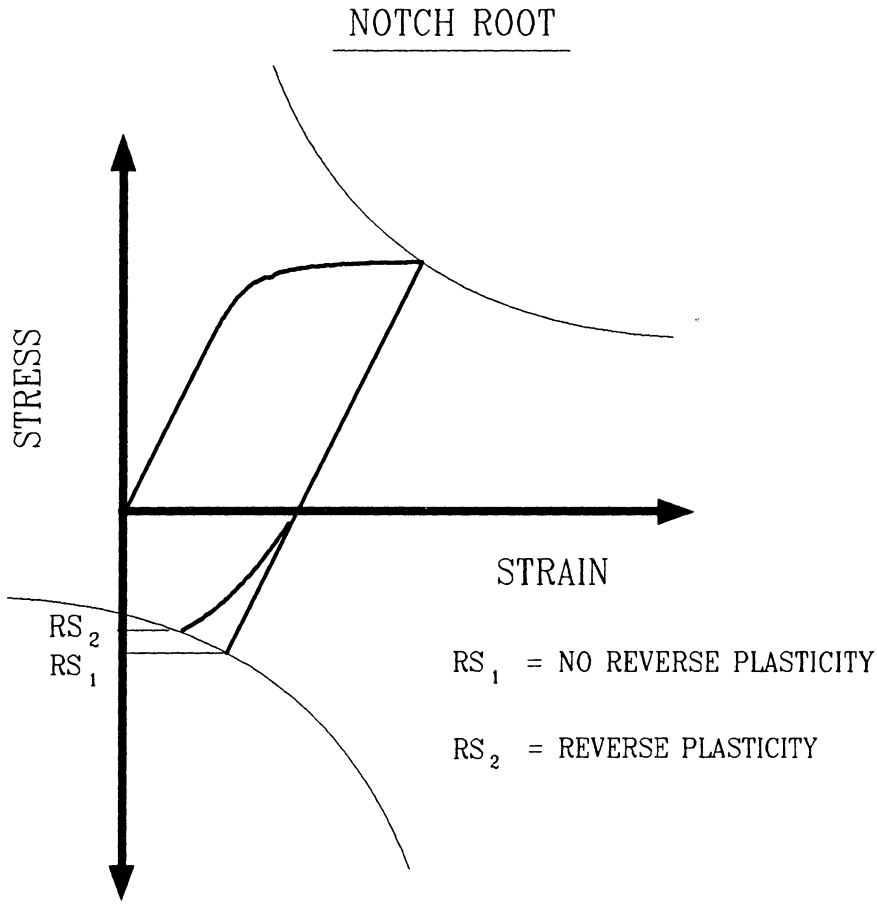

Figure 25. Effect of reverse plasticity on Neuber's Rule predictions of residual stress.

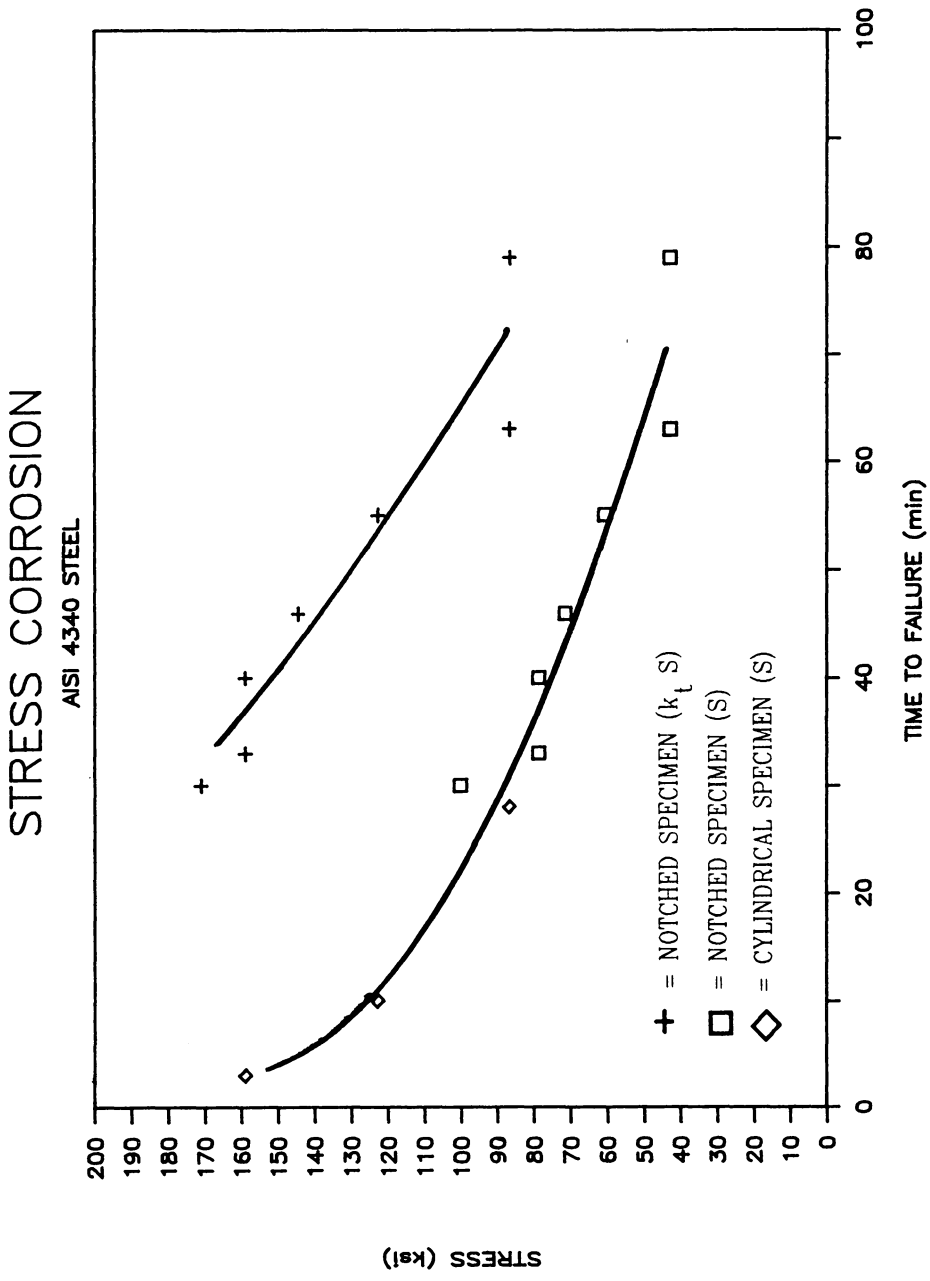

Figure 26. Results of SCC/HE tests for cylindrical and notched tensile specimens.

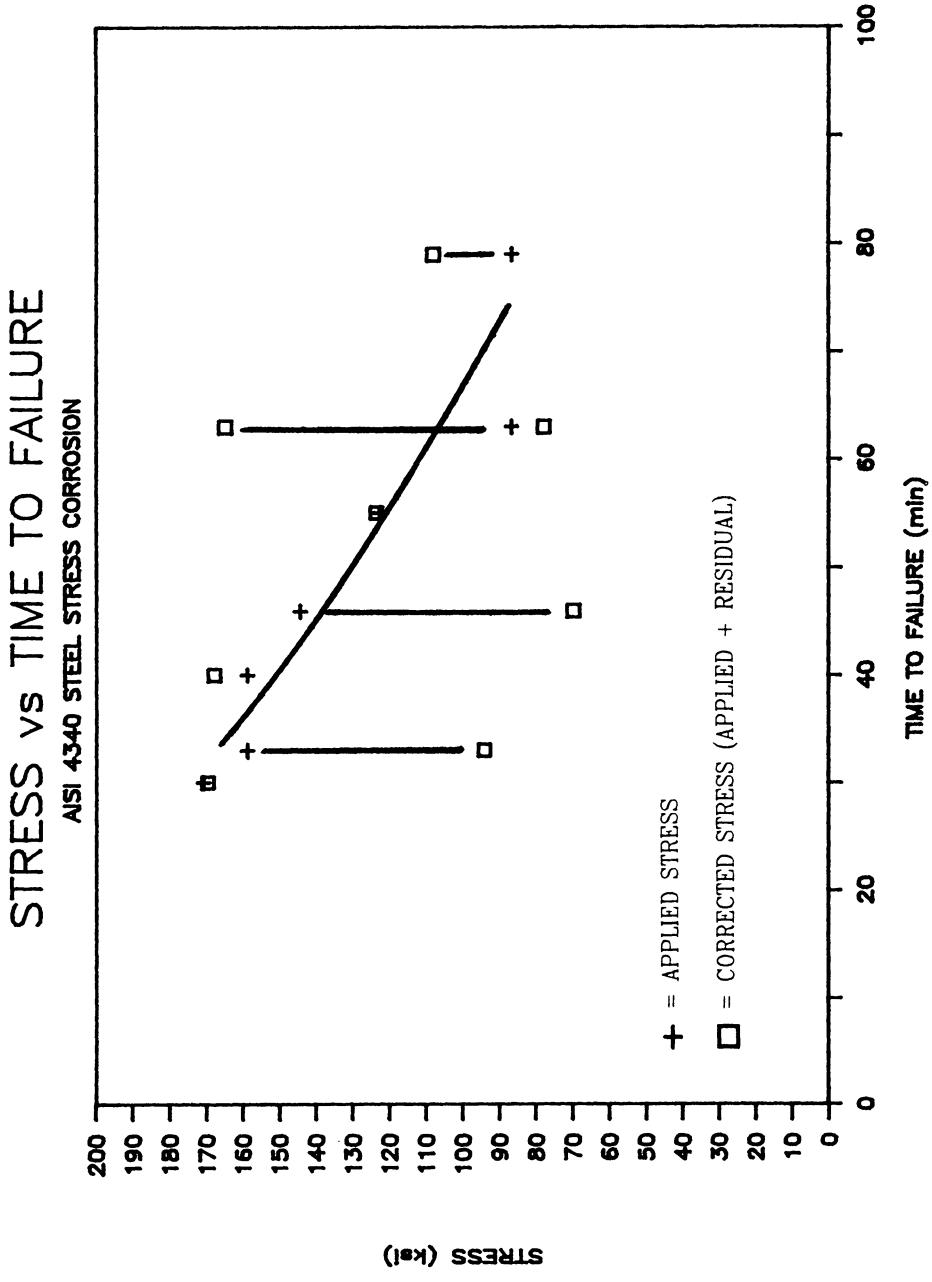

Figure 27. Comparison of applied stress and corrected stress versus time to failure for notched tensile specimens.

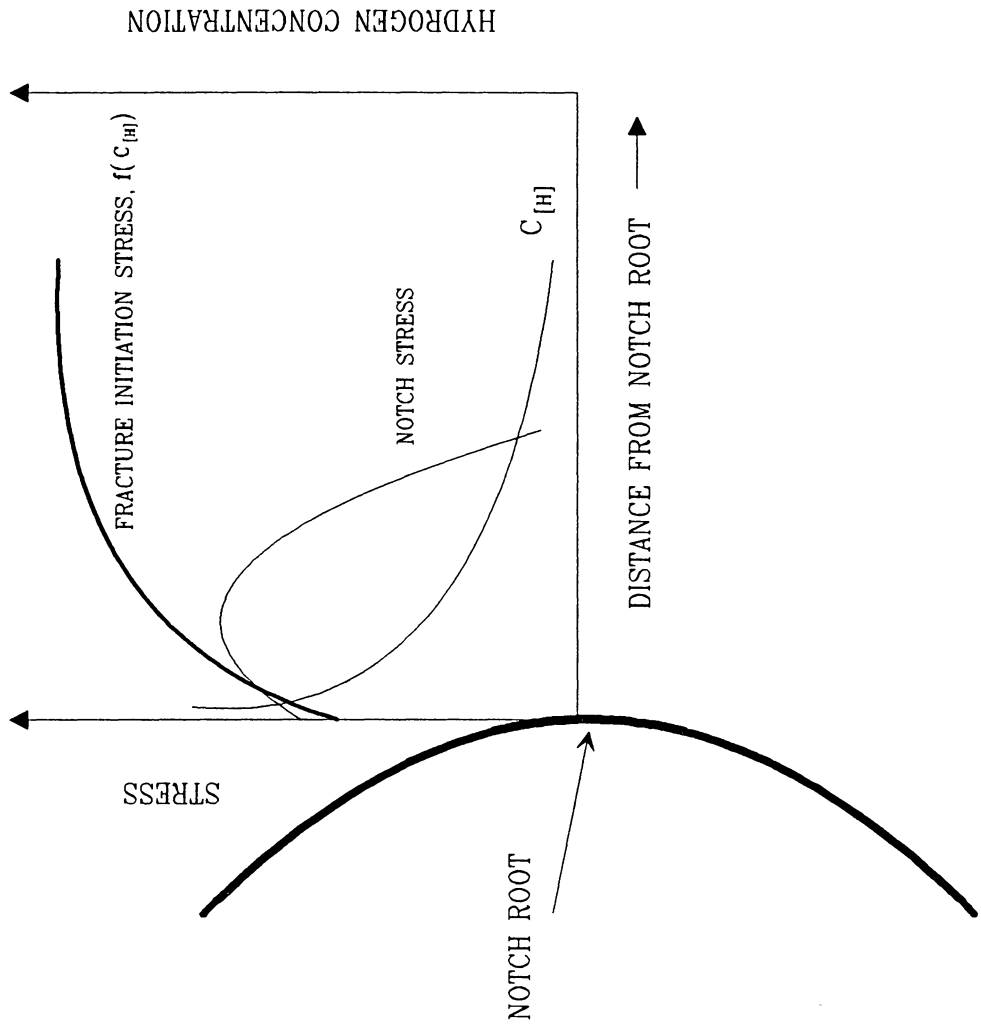

Figure 28. Schematic of surface crack initiation.

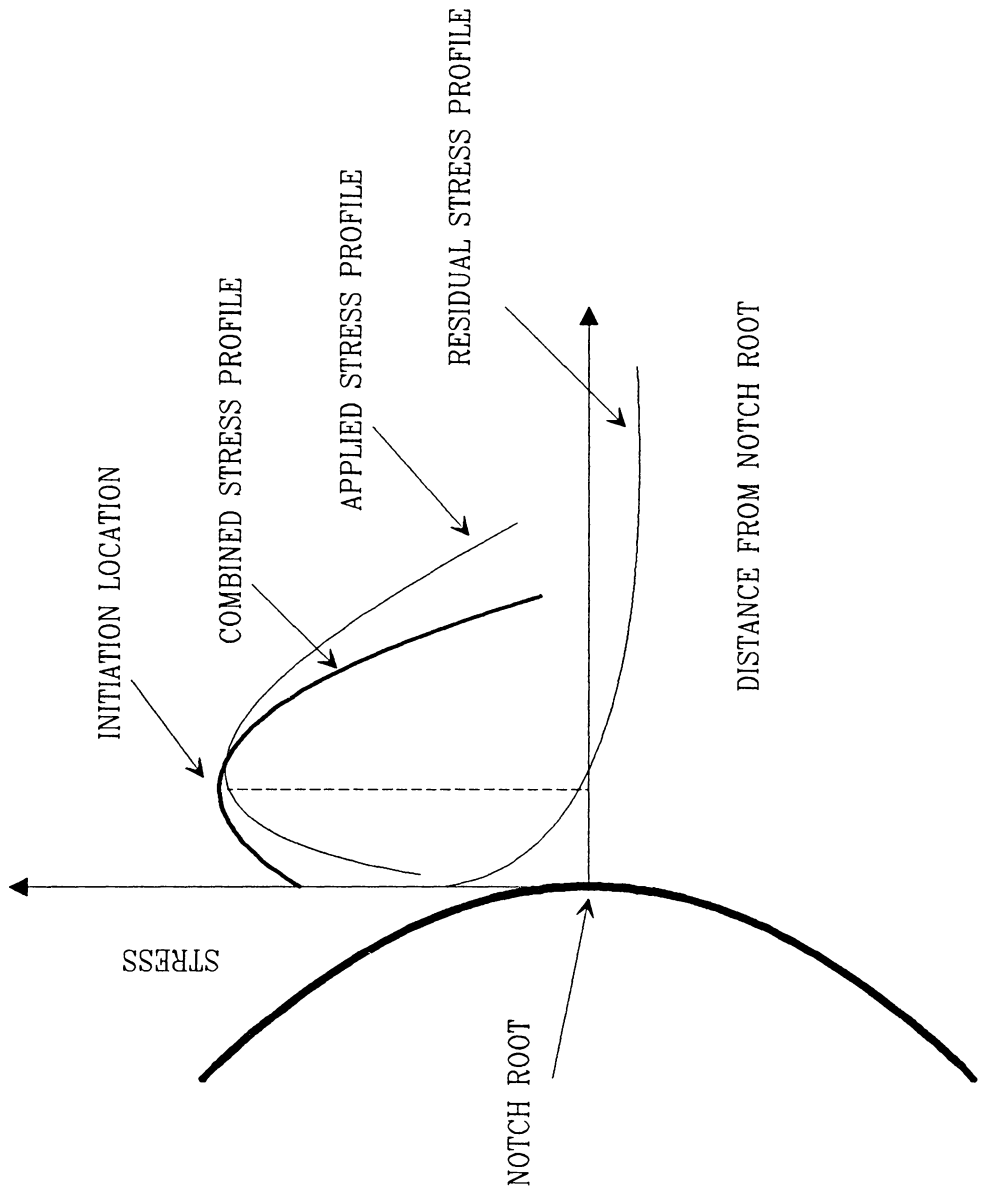

Figure 29. Schematic of subsurface crack initiation.

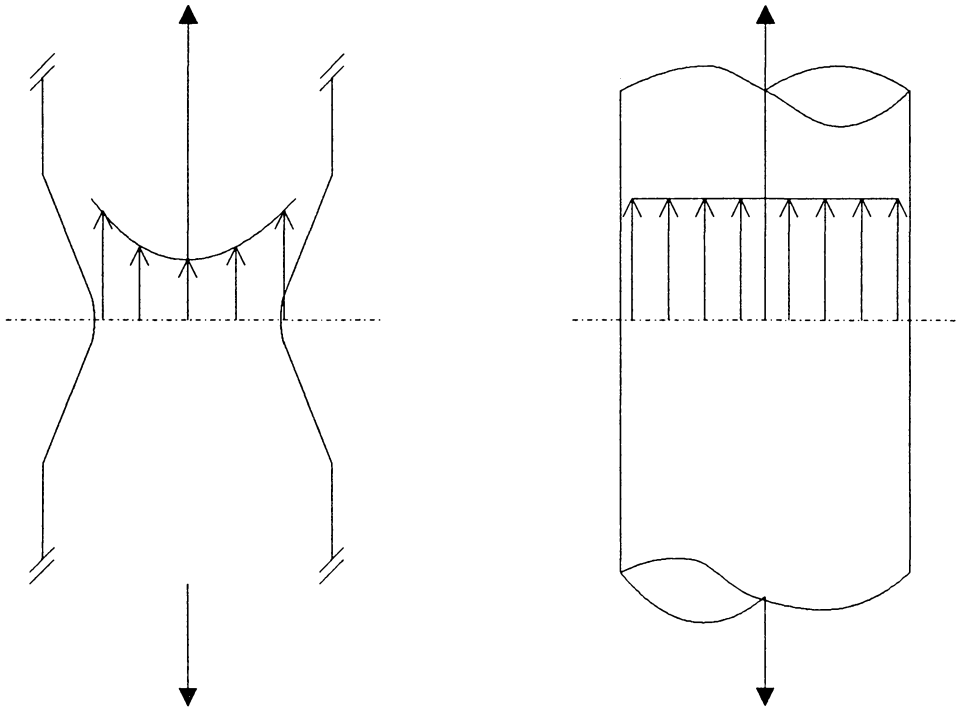

Notched Tensile Specimen

Cylindrical Tensile Specimen

Figure 30. Schematic of stress fields in cylindrical and notched tensile specimens.

The vita has been removed from the scanned document